NeuroImage 100 (2014) 145–160

Contents lists available at ScienceDirect

NeuroImage

journal homepage: www.elsevier.com/locate/ynimg

Matched-filter acquisition for BOLD fMRI

Lars Kasper [a,b,*], Maximilian Haeberlin [a], Benjamin E. Dietrich [a], Simon Gross [a], Christoph Barmet [a,c], Bertram J. Wilm [a], S. Johanna Vannesjo [a], David O. Brunner [a], Christian C. Ruff [d], Klaas E. Stephan [b,d,e], Klaas P. Pruessmann [a]

[a] Institute for Biomedical Engineering, University of Zurich and ETH Zurich, Switzerland
[b] Translational Neuromodeling Unit, Institute for Biomedical Engineering, University of Zurich and ETH Zurich, Switzerland
[c] Skope Magnetic Resonance Technologies, Zurich, Switzerland
[d] Laboratory for Social and Neural Systems Research (SNS), Department of Economics, University of Zurich, Switzerland
[e] Wellcome Trust Center for Neuroimaging, Institute of Neurology, University College London, United Kingdom

ARTICLE INFO

Article history:
Accepted 10 May 2014
Available online 17 May 2014

Keywords:
Matched-filter
fMRI
Image smoothing
BOLD sensitivity
Density-weighted EPI
Magnetic field monitoring

ABSTRACT

We introduce matched-filter fMRI, which improves BOLD (blood oxygen level dependent) sensitivity by variable-density image acquisition tailored to subsequent image smoothing. Image smoothing is an established post-processing technique used in the vast majority of fMRI studies. Here we show that the signal-to-noise ratio of the resulting smoothed data can be substantially increased by acquisition weighting with a weighting function that matches the k-space filter imposed by the smoothing operation. We derive the theoretical SNR advantage of this strategy and propose a practical implementation of 2D echo-planar acquisition matched to common Gaussian smoothing. To reliably perform the involved variable-speed trajectories, concurrent magnetic field monitoring with NMR probes is used. Using this technique, phantom and in vivo measurements confirm reliable SNR improvement in the order of 30% in a "resting-state" condition and prove robust in different regimes of physiological noise. Furthermore, a preliminary task-based visual fMRI experiment equally suggests a consistent BOLD sensitivity increase in terms of statistical sensitivity (average *t*-value increase of about 35%). In summary, our study suggests that matched-filter acquisition is an effective means of improving BOLD SNR in studies that rely on image smoothing at the post-processing level.

Introduction

Spatial smoothing of imaging volumes is ubiquitous in fMRI (Carp, 2012; Poldrack et al., 2008). Its routine use before statistical analysis aims at improving the sensitivity and interpretability of blood oxygen level dependent (BOLD) contrast in three ways, i.e., from the perspective of (1) signal processing, (2) statistical inference at the single-subject level and (3) group level inference (Friston, 2007).

Firstly, with respect to the signal processing perspective, smoothing the data with a filter that resembles the spatially extended hemodynamic response is considered optimal to detect activation of this particular shape and scale, according to the *matched-filter theorem* (Worsley et al., 1996a, b). Secondly, regarding single-subject inference, image smoothing facilitates the application of multiple comparison correction using random field theory (Worsley et al., 1996a, b) since it ensures spatial smoothness of the residual error distribution. Thirdly, at the group level, spatial smoothing helps to absorb anatomical variability between subjects.

Image smoothing is commonly performed with a filtering operation in k-space that attenuates signal content at high spatial frequencies. In doing so it alters the effective point spread function (PSF) such as to broaden its main peak and suppress far-range contamination. However, importantly, variable k-space attenuation not only affects the PSF but also the propagation of noise from raw data into smoothed images. The noise content of the raw data undergoes the same k-space weighting such that the relative impact of noise increases towards the center of k-space. As a consequence, to maximize the SNR of the smoothed data, the raw data should be acquired with variable sensitivity by corresponding k-space weighting at the acquisition level. As will be detailed in the theory part, optimal net SNR is achieved by acquisition weighting that exactly matches the eventual smoothing filter. The underlying mathematics correspond closely to the matched-filter rationale (North, 1963) of the smoothing operation. It is important, however, to distinguish the different filter-matching rationales. Aiming to match the hemodynamic response by smoothing is common practice today and serves for the purposes summarized initially. The utility of also matching data acquisition is a consequence of the smoothing strategy

Abbreviations: BOLD, Blood oxygen level dependent; EPI, Echo-planar imaging; EPSI, Echo-planar spectroscopic imaging; fMRI, Functional magnetic resonance imaging; FWHM, Full width at half maximum; PSF, Point spread function; SENSE, Sensitivity encoding; SFNR, Signal-to-fluctuation-noise ratio; TLS, Total least squares.

* Corresponding author at: Institute for Biomedical Engineering, University of Zurich and ETH Zurich, Gloriastrasse 35, ETZ F60.1, 8092 Zurich, Switzerland.
E-mail address: kasper@biomed.ee.ethz.ch (L. Kasper).

http://dx.doi.org/10.1016/j.neuroimage.2014.05.024
1053-8119/

and serves exclusively for SNR optimization given a chosen smoothing kernel. Importantly, through appropriate image reconstruction including density correction, the matched-filter acquisition does not change the PSF and thus allows for image post-processing that is identical to standard acquisition.

Acquisition weighting has previously been used to improve the sensitivity of MR spectroscopic imaging and non-proton MRI, summarized under the theme of density-weighted phase encoding (Greiser and von Kienlin, 2003; Greiser et al., 2005; Stobbe and Beaulieu, 2008). In this work, we introduce matched-filter acquisition for fMRI with single-shot echo-planar readouts, which is challenging in that it cannot be accomplished merely by altered phase encoding, but requires 2D trajectory design with complex modulation of k-space velocity. Such trajectories are particularly susceptible to common imperfections of gradient systems such as bandwidth limitations and eddy currents. To gauge and address this issue, we incorporate concurrent magnetic field monitoring (Barmet et al., 2008, 2009, 2010) with NMR probes (Barmet et al., 2010; De Zanche et al., 2008), which permits accounting for imperfections in magnetic field evolution at the image reconstruction stage.

The SNR benefit expected from filter matching relies on the incoherence of noise. In particular, the exact form of the matched-filter acquisition rule proposed here refers to the assumption of independent and identically distributed white noise. Thermal noise, which is prevalent in MR, exhibits this property (Johnson, 1928; Nyquist, 1928). For this noise regime, we show analytically that the distribution of acquisition time should indeed exhibit the same weighting in k-space as the target PSF, to achieve maximum SNR. However, BOLD fMRI is also subject to noise related to physiological processes with non-white statistics (Bianciardi et al., 2009; Krüger and Glover, 2001), including inherent neurophysiological fluctuations as well as respiratory and cardiovascular dynamics (Birn et al., 2008; Chang et al., 2009; Dagli et al., 1999; Glover et al., 2000; Shmueli et al., 2007). Therefore, the experimental validation of matched-filter fMRI in this work comprises signal-to-fluctuation-noise ratio (SFNR) measurements of phantom and in vivo time series, in which we vary the degree of signal-mediated fluctuations and evaluate their influence on the observed SFNR gain. Finally, we perform a proof-of-principle experiment showing the feasibility of matched-filter acquisition also for task-based fMRI. Using a visual paradigm in a preliminary group of four subjects, robust t-value increases are reported over standard EPI acquisition.

Theory and methods

Theory: Matched-density acquisition for image post-processing filters

In the following section, we establish the relationship between variable acquisition speed in k-space, the point-spread function (PSF) and signal-to-noise ratio (SNR) within an MR image. This is contrasted to shaping the PSF by retrospective smoothing only.

To estimate SNR, we consider the different propagation of signal and noise in both stages, focusing on the total thermal noise contribution similar to Pipe and Duerk (1995) and Stobbe and Beaulieu (2008), but treating all quantities in a continuous fashion, which then leads to a variational optimization of SNR.

Accrual of signal and noise in a given k-space region depends on how much acquisition time is spent in that region. If local acquisition time is distributed non-uniformly, it becomes dependent on the k-space position vector $\boldsymbol{k} = (k_x, k_y k_z)$. Hence, we denote the resulting distribution of acquisition time as *acquisition density* $d_{\mathrm{acq}}(\boldsymbol{k})$ Upon gridding reconstruction, d_{acq} becomes effectively smooth on the scale of the Nyquist sampling interval and represents the local density of trajectory segments and their velocity.

Signal accrues coherently over time and thus linearly with $d_{\mathrm{acq}}(\boldsymbol{k})$. Thermal noise, on the other hand, accrues incoherently because it is uncorrelated due to being identically, independently normally distributed (Johnson, 1928; Nyquist, 1928). Hence, the *variance* of the thermal noise increases linearly with local acquisition density:

$$\sigma^2_{\mathrm{acq}}(\boldsymbol{k}) \propto d_{\mathrm{acq}}(\boldsymbol{k}). \tag{1}$$

Let us now consider smoothing during post-processing which is performed to achieve a target PSF. As the combined action of smoothing and acquisition weighting in k-space should yield the target density, we obtain a defining equation for the smoothing filter:

$$d_{\mathrm{smooth}}(\boldsymbol{k}) := \frac{d_{\mathrm{target}}(\boldsymbol{k})}{d_{\mathrm{acq}}(\boldsymbol{k})} \tag{2}$$

with d_{target} and d_{smooth} being the Fourier transform of the PSF and smoothing kernel, respectively.

We now investigate the action of this post-processing filter on the acquired k-space data, which is already a superposition of signal and noise. The application of $d_{\mathrm{smooth}}(\boldsymbol{k})$ is a mere re-weighting of these data. Thus, the signal scales linearly with this density as in the case of acquisition weighting. The noise amplitude, however, is now also proportionally scaled with this density, inducing a quadratic dependency of the noise variance on d_{smooth} in the final, post-processed data,

$$\sigma^2_{\mathrm{final}}(\boldsymbol{k}) = d^2_{\mathrm{smooth}}(\boldsymbol{k}) \cdot \sigma^2_{\mathrm{acq}}(\boldsymbol{k}) \propto d^2_{\mathrm{smooth}}(\boldsymbol{k}) \cdot d_{\mathrm{acq}}(\boldsymbol{k}) = \frac{d^2_{\mathrm{target}}(\boldsymbol{k})}{d_{\mathrm{acq}}(\boldsymbol{k})}, \tag{3}$$

where equality and proportionality arise from Eqs. (1) and (2), respectively.

This equation illustrates that the acquisition density is an additional degree of freedom for an MR experiment with a given target PSF, because the target PSF can always be achieved retrospectively by smoothing with an appropriate image filter K_{smooth}. The choice of the acquisition density, on the other hand, then determines the noise landscape in k-space, $\sigma^2_{\mathrm{final}}$ for the final, reconstructed image, as described in Eq. (3).

Given a specific target PSF, an immediate application of Eq. (3) is to find the acquisition density that maximizes SNR in the image. As long as Nyquist sampling is ensured, the signal level is independent of d_{acq}, because it is determined by the target PSF (which is the same for all acquisition densities). Thus, to maximize SNR, it suffices to minimize the noise variance in each image voxel. As we reconstruct an image from the acquired k-space data of an individual coil through Fourier transformation and the thermal noise accrued in k-space is uncorrelated, the noise landscape in the conjugate image space will be flat according to the Wiener-Khinchin theorem (Weisstein, 2006b), rendering all voxel noise variances in the image equal. Minimizing the noise variance per voxel is therefore equivalent to minimizing the total noise power in the image which, in turn, is equivalent to the noise power in k-space due to Parseval's theorem (Weisstein, 2006a).

Hence, maximizing the SNR per voxel amounts to a constrained minimization of the noise power in the covered k-space volume V_k which we define as

$$|\sigma_{\mathrm{final}}|_2^2 := \int_{V_K} \sigma^2_{\mathrm{final}}(\boldsymbol{k})\, \mathrm{d}\boldsymbol{k}. \tag{4}$$

The optimization constraint is given by a constant total acquisition time T_{acq}, such that the full optimization problem incorporating relation (3) reads

$$|\sigma_{\mathrm{final}}|_2^2 = \int_{V_k} \frac{d^2_{\mathrm{target}}(\boldsymbol{k})}{d_{\mathrm{acq}}(\boldsymbol{k})} \mathrm{d}\boldsymbol{k} \rightarrow \min \text{ with } \int_{V_k} d_{\mathrm{acq}}(\boldsymbol{k})\, \mathrm{d}\boldsymbol{k} = T_{\mathrm{acq}}. \tag{5}$$

The solution to this optimization uses a Lagrange multiplier λ and fulfills

$$\frac{\partial\left(|\sigma_{\text{final}}|_2^2\right)}{\partial\left(d_{\text{acq}}(\boldsymbol{k})\right)} = \lambda\frac{\partial \int d_{\text{acq}}(\boldsymbol{k})\,\text{d}\boldsymbol{k}}{\partial\left(d_{\text{acq}}(\boldsymbol{k})\right)} \Rightarrow -\frac{d_{\text{target}}^2(\boldsymbol{k})}{d_{\text{acq}}^2(\boldsymbol{k})} = \lambda\cdot\text{const.} \qquad (6)$$
$$\Rightarrow d_{\text{acq}}(\boldsymbol{k}) \propto d_{\text{target}}(\boldsymbol{k})$$

Therefore, for optimal SNR, target density and acquisition density should be equal in k-space (up to a proportionality factor), in analogy to the *matched-filter* theorem (Fig. 1; North, 1963). Specifically, in the common case where the target PSF is a Dirac function that maps the object onto image pixels identically, uniform sampling is optimal (Pipe and Duerk, 1995).

The SNR ratio between a matched acquisition and the standard uniform sampling can be expressed via the ratio of final noise variances, i.e.,

$$\frac{SNR_{\text{final}}^{\text{matched}}}{SNR_{\text{final}}^{\text{uni}}} = \sqrt{\frac{\left|\sigma_{\text{final}}^{\text{uni}}\right|_2^2}{\left|\sigma_{\text{final}}^{\text{matched}}\right|_2^2}}. \qquad (7)$$

We now simplify the numerator and denominator of the right hand side term separately using Eq. (5). For the square of the numerator, the acquisition density fulfills $\int_{V_k} d_{\text{acq}}(\boldsymbol{k})\text{d}\boldsymbol{k} = T_{\text{acq}}$, while the uniform sampling density reads $d_{\text{uni}}(\boldsymbol{k}) = T_{\text{acq}}/V_K = \text{const.}$, yielding

$$\left|\sigma_{\text{final}}^{\text{uni}}\right|_2^2 = \int_{V_k} \frac{d_{\text{target}}^2(\boldsymbol{k})}{\frac{T_{\text{acq}}}{V_k}}\text{d}\boldsymbol{k} = \frac{V_k}{T_{\text{acq}}}\int_{V_k} d_{\text{target}}^2(\boldsymbol{k})\text{d}\boldsymbol{k}. \qquad (8)$$

We normalize the matched acquisition density to $d_{\text{matched}}(\boldsymbol{k}) = C^{-1}\cdot T_{\text{acq}}\cdot d_{\text{target}}(\boldsymbol{k})$ with $C := \int_{Vk} d_{\text{target}}(\boldsymbol{k})\,\text{d}\boldsymbol{k}$, and, hence, can rewrite the square of the denominator of Eq. (7):

$$\left|\sigma_{\text{final}}^{\text{matched}}\right|_2^2 = \int_{V_k} \frac{d_{\text{target}}^2(\boldsymbol{k})}{C^{-1}\cdot T_{\text{acq}}\cdot d_{\text{target}}(\boldsymbol{k})}\text{d}\boldsymbol{k} = \frac{1}{C^{-1}\cdot T_{\text{acq}}}\underbrace{\int_{V_k} d_{\text{target}}(\boldsymbol{k})\text{d}\boldsymbol{k}}_{=C}. \qquad (9)$$

The SNR ratio between matched and uniform acquisition then evaluates to

$$\frac{SNR_{\text{final}}^{\text{matched}}}{SNR_{\text{final}}^{\text{uni}}} = \sqrt{\frac{\left|\sigma_{\text{final}}^{\text{uni}}\right|_2^2}{\left|\sigma_{\text{final}}^{\text{matched}}\right|_2^2}} = \sqrt{\frac{\frac{V_k}{T_{\text{acq}}}\int_{V_k} d_{\text{target}}^2(\boldsymbol{k})\text{d}\boldsymbol{k}}{\frac{C^2}{T_{\text{acq}}}}} = \sqrt{\frac{V_k}{C^2}\cdot\int_{V_k} d_{\text{target}}^2(\boldsymbol{k})\text{d}\boldsymbol{k}}, \qquad (10)$$

and is therefore proportional to the 2-norm of the target density.

For the fMRI application under consideration, the SNR gain can be explicitly calculated given the ratio between the nominal resolution before smoothing and the FWHM of the Gaussian target PSF, as derived formally in Appendix A. The result is an intrinsic SNR gain capturing the situation of ideal density weighting, which, in practice, is limited by the fidelity of the gradient system. Typical choices of the

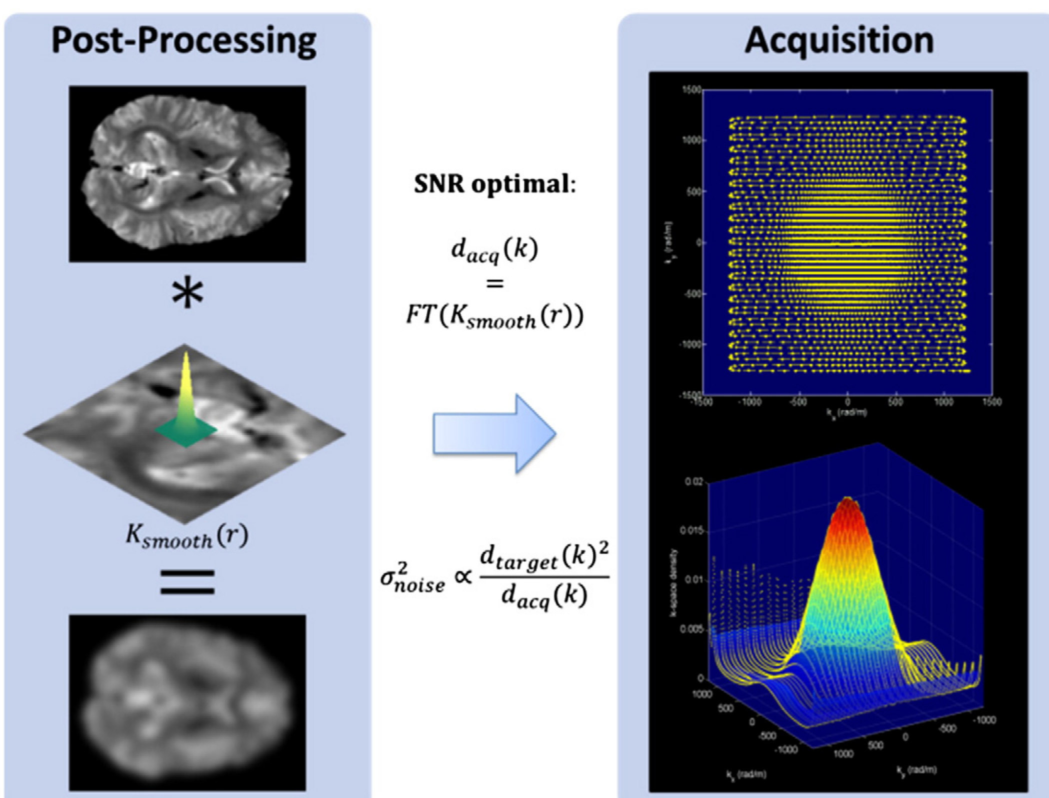

Fig. 1. The concept of matched-filter acquisition: After identifying the target post-processing filter K_{smooth} of a statistical analysis, a corresponding k-space trajectory is designed for image acquisition. Following the matched-filter theorem, this trajectory delivers SNR optimal images, if its variable k-space acquisition density d_{acq} is equivalent to the Fourier transform of the target post-processing filter.

Table 1
Theoretical SNR gains expected for a matched-filter 2D acquisition of a Gaussian target PSF for different values of its full width at half maximum (FWHM). The intrinsic SNR gain refers to a perfect realization of a Gaussian acquisition density, while the reference experiment values are calculated for the designed matched-filter EPI trajectory constrained by typical gradient amplitude and slew rate system limits.

FWHM of target PSF in nominal pixels	1	1.5	2	2.5	3	3.5	4
SNR gain (2D)Intrinsic	6%	23%	53%	88%	126%	163%	201%
SNR gain (2D)Reference Experiment	3%	12%	25%	40%	55%	72%	92%

Gaussian FWHM deliver an intrinsic SNR gain of 2D matched-filter compared to uniform acquisition between 6% and 200% (see Table 1) that depends approximately linearly on the FWHM of the Gaussian kernel.

Intuitively, this linear dependence of SNR gain on FWHM can be understood as follows: Acquisition time is spent inefficiently by uniform sampling in areas of k-space where the target density weighting is low, because noise is accumulated, but the signal information is hardly used. This area shrinks quadratically with the FWHM of the target k-space density and therefore increases quadratically with the FWHM of the target PSF. Thus, the additional standard deviation in the final image increases linearly with this FWHM of the target PSF due to uniform sampling.

Theory: EPI trajectory design for a matched-filter Gaussian density

As a k-space trajectory is needed for MR image encoding, we now show how to transform the target acquisition density obtained in the last section into a continuous trajectory subject to gradient system limitations. Specifically, we design a single-shot Gaussian acquisition density 2D EPI trajectory to enable a direct comparison with the most prominent fMRI acquisition technique, i.e., a 2D EPI with uniform acquisition density.

In principle, the k-space acquisition density can be altered by two aspects of trajectory specification: Firstly, the shape of the trajectory can be modified by variable spacing of different trajectory segments, such as EPI traverses or spiral revolutions (Greiser and von Kienlin, 2003; Greiser et al., 2005; Kim et al., 2003; Spielman et al., 1995). Secondly, the velocity along the trajectory can be modulated, thus distributing acquisition time variably in k-space.

For EPI, modifying the trajectory shape could be readily implemented by only modulating the density of traverses. A variable time allocation would be accomplished, as more acquisition time is allocated to regions with relatively more traverses. On the downside, more traverses would accrue more traverse turns locally, such that too much acquisition time is deployed compared to the Nyquist sampling density needed. To minimize the number of such turns, the general objective of an effective trajectory design is to pay as few separate visits to the same k-space region as possible. Consequently, as reducing the number of turns would violate Nyquist sampling, it is best to perform density weighting for single-shot EPIs via velocity modulation exclusively.

The Gaussian kernel is separable, therefore the density weighting in k_x and k_y can be designed independently. First, we will determine the acquisition weighting within a single EPI traverse, i.e. along k_x: Because gradient strength is proportional to k-space speed, it is inversely proportional to the time spent in this particular part of k-space and therefore to the acquisition density (cf. Eq. (1)). The ideal k-space (and gradient) evolution $k(t)$ $(G(t))$ then solves the following differential equation (γ being the gyromagnetic ratio for protons):

$$d_{\mathrm{acq}}(k) \propto \frac{1}{|\dot{k}|} = \frac{1}{\gamma \cdot |G(t)|}. \tag{11}$$

If the acquisition density is Gaussian, a closed form solution exists for this equation, whose derivation can be found in Appendix B. With the nominal resolution Δx determining $k_{\max} = \frac{\pi}{\Delta x}$ and the FWHM of the smoothing kernel defining $\sigma_r = \mathrm{FWHM}/\sqrt{8 \ln 2}$, one obtains:

$$G(t) = C_1 \cdot \exp\left(\mathrm{erf}^{-1}\left(C_2 \cdot \left(2 \frac{t}{T_{\mathrm{traverse}}} - 1 \right) \right)^2 \right)$$
$$\text{With } C_1 = \frac{\sqrt{2\pi} \cdot \mathrm{erf}\left(\frac{\sigma_r k_{max}}{\sqrt{2}} \right)}{\gamma T_{\mathrm{traverse}} \sigma_r}, \text{ and } C_2 = \mathrm{erf}\left(\frac{\sigma_r k_{\max}}{\sqrt{2}} \right). \tag{12}$$

In practice, due to gradient amplitude and slew rate limitations, this time course cannot be realized at the traverse turns which require the fastest possible gradient switching.

To achieve a Gaussian density weighting along the phase encoding direction, k_y, we vary the acquisition time spent on different traverses, T_{traverse}: While the gradient shape follows Eq. (12) for all traverses, the scaling factor C_1 of the gradient amplitude depends on the k_y-coordinate of the specific traverse, according to Eqs. (6) and (12):

$$C_1 \propto \frac{1}{T_{\mathrm{traverse}}\left(k_y\right)} \propto \frac{1}{d_{\mathrm{target}}\left(k_y\right)} \propto \exp\left(\frac{k_y{}^2 \sigma_r^2}{2} \right). \tag{13}$$

For traverses where C_1 exceeds the maximum gradient amplitude, the Gaussian acquisition density is replaced by a baseline uniform density ensuring Nyquist sampling.

This method for designing a Gaussian density 2D EPI trajectory may be applied to arbitrary fields of view, resolutions and readout acquisition times. Furthermore, parallel imaging acceleration in phase encoding direction can be implemented simply by increasing the constant spacing between EPI traverses. The matched-filter considerations, including the expected SNR gain, equally apply to the parallel imaging case since parallel imaging reconstruction is highly local in k-space and the Gaussian acquisition density is smooth, i.e. approximately constant locally.

Due to the finite acquisition time and gradient system limitations, the matched-filter EPI trajectory implemented as such does not lead to a perfect Gaussian acquisition density. Strictly speaking, a standard EPI trajectory does not implement a uniform acquisition density either due to the traverse turns mentioned above which over-emphasize high spatial frequencies.

Therefore, the expected reference SNR gain must be calculated specifically for the matched-filter and uniform EPI trajectory implemented by inserting their actual acquisition densities into Eqs. (5) and (7). For the imaging parameters and gradient specifications reported in the subsequent section, the reference SNR gain reaches approximately half of the intrinsic SNR gain referring to ideal density weighting (Table 1), i.e., about 40% for a typically chosen Gaussian FWHM of 2.5 voxels.[1]

Image acquisition, concurrent field monitoring and image reconstruction

For all our experiments, data were acquired on a Philips 3 T Achieva (Best, The Netherlands) system equipped with an 8-channel head coil (Philips, Best, The Netherlands) and gradient specifications of 31 mT/m maximum amplitude and 200 T/m/s maximum slew rate. We compared a matched-filter EPI to a uniform EPI trajectory that shared the following acquisition parameters: TR 3 s (phantom data: 6.25 s), TE 35 ms, readout duration 41 ms, receiver bandwidth 375 kHz, FOV 227 mm, SENSE reduction factor 3, voxel size $1.8 \times 1.8 \times 3$ mm^3, 5 slices with 3 mm between-slice gap. The target filter was a 2D Gaussian with a FWHM of 4.5 mm (or 2.5 voxels).

[1] According to a recent meta-study on 300 fMRI studies (Carp, 2012), 88% of all studies reported using (presumably Gaussian) smoothing, and nearly more than half of them with a FWHM of 8 mm and larger, which corresponds to more than 2.5 pixels for voxel sizes of 3 mm and below.

We deliberately designed the uniform EPI to have the same readout duration as the matched-filter EPI (41 ms), although the gradient specifications would have allowed for a faster uniform readout (29 ms), and hence, more volumes per time. This prolonged readout enabled a fair SFNR comparison to the matched-filter trajectory, because the increase in temporal SNR when decreasing slice TR $\approx$ TE + $T_{acq}/2$ from 56 to 50 ms is outweighed by the SNR loss per image when decreasing image acquisition time from 41 to 29 ms.

Separate B_0 and coil receive sensitivity maps were acquired in each session (TR 800 ms, TE_1 1 ms, $\Delta TE = 2.3$ ms, spin-warp images with a resolution of $1 \times 1 \times 3$ mm^3).

Our implementation of the matched-filter Gaussian EPI trajectory using variable gradient strengths is particularly susceptible to any kind of gradient imperfections. There are two reasons for this sensitivity: On the one hand, the gradient system is operated close to its limits to enable a large range of velocity modulation. On the other hand, the non-periodic gradient time course precludes standard correction methods for gradient inaccuracies, such as EPI phase correction. Therefore, we utilized concurrent magnetic field monitoring as introduced by Barmet et al. (2008, 2009, 2010, 2011) to (1) investigate the feasibility and accuracy of the demanding gradient evolutions of the proposed matched-filter EPIs on a clinical MR system, (2) study deviations in k-trajectories and k-space densities from the ideal matched-filter EPI and (3) enable image reconstructions informed by the actual, measured k-space trajectory. In the hetero-nuclear monitoring setup 16 transmit/receive ^{19}F NMR field probes were attached to the head coil (Barmet et al., 2010; De Zanche et al., 2008; Wilm et al., 2011). The acquired probe phase evolutions were expanded into real-valued spherical harmonics (Barmet et al., 2008; Vannesjo et al., 2013b; Wilm et al., 2011), yielding phase coefficients for the global phase, $k_0(t)$, the linear k-space, $k_x(t)$, $k_y(t)$ and $k_z(t)$ and second order phase coefficients $k_{4\text{-}8}(t)$ over the entire readout.

All image reconstructions, for both matched-filter and uniform EPI, were performed using concurrent field monitoring data from the probe phase fits. Global (k_0) phase information was used for demodulation of the raw coil data of the 8-channel head coil. Afterwards, the images were reconstructed from the demodulated data in combination with 1st order k-space trajectory information (k_x, k_y, k_z) in an iterative, gridding-based, conjugate-gradient SENSE algorithm (Beatty et al., 2005; Jackson et al., 1991; Pruessmann et al., 2001), using an in-house Matlab implementation (The MathWorks, Natick, MA). This algorithm was augmented with multi-frequency interpolation (MFI) for static B_0-field correction (Man et al., 1997; Sutton et al., 2003). The application of this reconstruction algorithm ensured an SNR optimal image reconstruction where the target PSF was achieved post hoc via smoothing, which is equivalent to direct reconstruction with the target PSF (Pruessmann and Tsao, 2008). In particular, the objective function of the reconstruction imposed a Dirac target PSF, thus performing an implicit density correction for the variable acquisition density of the matched-filter trajectory. Consequently, both matched-filter and uniform EPI scans exhibited the same image resolution and smoothness before entering statistical pre-processing.

Experiment 1: Assessment of SFNR gain for EPI time series in different noise regimes

The first experiment assessed the validity of the matched-filter acquisition argument for different noise regimes with different levels of signal fluctuations. Phantom data were acquired from a water-filled sphere. In vivo data were acquired from 4 healthy volunteers (1 male) after written informed consent and with approval of the local ethics committee. Subjects were asked to lie still in the scanner with their eyes closed (i.e., a "resting-state" condition).

For both uniform and matched-filter EPI, we acquired 9 sessions with different excitation flip angles (0, 5, 15, 25, 40, 50, 60, 75 and 90 degrees) to vary the signal content and therefore the contribution of signal-dependent noise. Each session contained 95 scans for the phantom data, and 48 scans for in vivo sessions, plus 5 void scans to minimize saturation effects. Realignment and smoothing with the matched target kernel were performed on all images using SPM8 (http://www.fil.ion.ucl.ac.uk/spm/).

We considered SFNR ROI-wise by first determining the mean of the magnitude signal within the ROI for each image. Then, the SFNR was computed as the ratio of the temporal mean of this ROI mean and its temporal standard deviation. The ROI in the phantom was a centered disc in each slice extending to 2/3 of the object diameter to avoid edge effects. For the in vivo case, subject-specific gray matter, white matter and CSF regions—that suffer from different levels of physiological noise (Krüger and Glover, 2001; Triantafyllou et al., 2006)—were included as separate ROIs in the analysis. These regions were extracted using B_1 bias field correction (Salvado et al., 2006) and a k-means clustering algorithm on the spin-warp TE_1 image.

Experiment 2: fMRI paradigm and analysis

In the second experiment, the benefits of matched-filter EPI acquisition were assessed in a visual fMRI paradigm using *t*-contrast values as a summary statistic of activation detection.

The fMRI paradigm was designed to stimulate the quarter-fields of the visual cortex: 16 s of flickering, color-changing wedges were interleaved with 5 s of fixation; 8 blocks of upper left/lower right (ULLR) and upper right/lower left (URLL) wedges were presented over 120 scans (TR 3 s). The visual presentation was performed using a projector (resolution 800×600) and a mirror mounted on the head coil. Subjects' attention was maintained using a simple button response task to any contrast alteration of the fixation point.

The data were acquired in the same subjects and—apart from subject 4—on the same measurement day as for experiment 1. Two sessions of each uniform EPI and matched-filter EPI acquisition were measured to compare within-modality variance to between-modality variance of the statistical results. The order of matched and uniform acquisitions was counterbalanced between subjects, and independently for the 1st and 2nd repetition of these sessions. The slice geometry was equivalent to experiment 1. Specifically, slice orientation was oblique transverse, parallel to the calcarine sulcus to cover visual cortex. Peripheral physiological measures characterizing cardiac pulsation and the respiratory cycle were recorded simultaneously with fMRI using an electrocardiogram (ECG) and breathing belt, respectively.

Spatial preprocessing and statistical analysis of the fMRI data were performed in SPM8. Pre-processing included realignment and spatial smoothing with the target Gaussian PSF. The general linear model (GLM) for the statistical analysis included a canonical hemodynamic response function (HRF) and temporal/dispersion derivative regressors of the ULLR and URLL blocks. Furthermore, we included 2 types of nuisance regressors into the GLM: 6 movement parameters from realignment and physiological noise modeling using RETROICOR (Glover et al., 2000). Our specific implementation of RETROICOR, the physIO Toolbox (Kasper et al., 2009; open source code available as part of the TAPAS software collection: http://www.translationalneuromodeling.org/tapas/) uses Fourier expansions of different order for the estimated phases of cardiac pulsation (3rd order), respiration (4th order) and cardiorespiratory interactions (1st order) following (Harvey et al., 2008).

The statistical results were assessed on *t*-maps contrasting ULLR–URLL (contrast 1) and URLL–ULLR (contrast 2). Both peak *t*-value and total cluster sizes were compared between matched and uniform acquisition sessions. All results were $p = 0.05$ FWE-peak level corrected for the whole acquisition volume. Finally, for a more quantitative handle on BOLD sensitivity, we performed a total least squares regression (TLS, modified Matlab implementation; Hall, 2011) of all corresponding brain voxels for the *t*-value change of one session compared to a reference session. TLS reports an average *t*-value change over all voxels, and thus a more robust summary measure than peak *t*-values or activation extent.

Results

Monitoring: Trajectories and k-space densities

For the implemented matched-filter EPI, the concurrently monitored encoding magnetic fields, phase coefficients and corresponding k-space densities are shown in Figs. 2–4, respectively. We present the measured matched-filter readout for the representative 5th scan of the 1st fMRI session of subject 3, but the asserted statements hold for all observed readouts.

In general, the demanding non-trapezoidal readout gradient waveform is reproduced quite accurately by the gradient system, exhibiting only the common bandwidth limitation of the gradients, smoothing of switching events and small gradient delays (Fig. 2, red curve, compared to black curve of nominal gradient evolution). Note that the amplitude of the measured phase encoding gradient blip is also greatly reduced due to this low-pass filter property of the gradient chain (Fig. 2B), but its area is preserved due to commensurate broadening of the blip (cf. the EPI traverse spacing in Fig. 4A.)

Fig. 3 shows the phase evolutions induced by this gradient waveform expanded in 0th to 2nd spatial order spherical harmonics: For the monitored global phase k_0, a roughly linear increase during the readout is evident that carries the distinct sinusoidal modulation of the EPI traverses (about 300 Hz). This modulation presumably stems from slight B_0 eddy currents induced by the readout gradient. Similarly, the reduced slope of the linear component of k_0 during the central part of the readout might result from the lower frequency of phase encoding gradients and their concomitant B_0 eddy currents for the inner, density-weighted traverses.

The linear phase coefficients (Fig. 3, middle panel), i.e. the k-space representation of the trajectory, exhibit two main deviations from the nominal matched-filter EPI, which are best visible in the classical 2D representation of the trajectory (Fig. 4): Firstly, we found a compression of about 25 rad/m of the trajectory in frequency encoding direction, resulting in a slightly reduced actual image resolution, which has also been reported for uniform EPI trajectories (Vannesjo et al., 2013b). Secondly, the actual sampling points within the traverse did not coincide exactly with the nominal positions but deviated by up to one Nyquist sampling interval in frequency encoding direction (Fig. 4, zoomed panels).

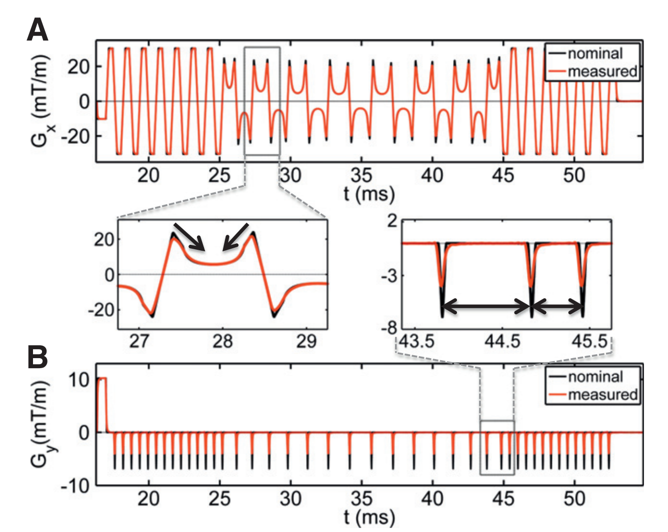

Fig. 2. Gradient design and concurrent field monitoring results of a 2D Gaussian density-weighted "matched-filter" EPI. (A) Intra-traverse weighting via gradient modulation in readout-direction (black = nominal; red = measured). (B) Inter-traverse weighting via variable traverse duration in phase-encoding direction.

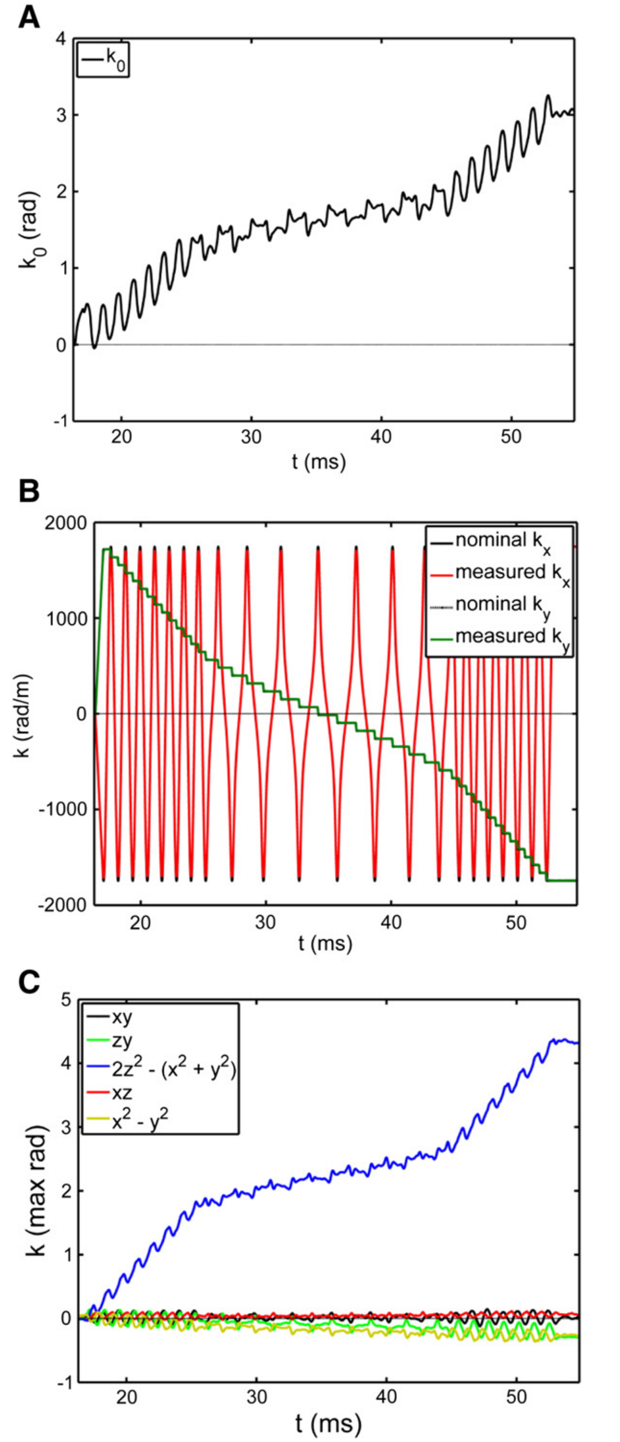

Fig. 3. Measured phase evolution during a matched-filter EPI readout of 40 ms (TE 35 ms). Shown are the spherical harmonics coefficients *k* of different spatial order retrieved by concurrent magnetic field monitoring. (A) 0th order phase coefficient: A linear component (frequency offset) is modulated by the EPI traverse frequency as well as the density weighting close to the echo time. (B) 1st order phase coefficients in readout (k_x, red line) and phase direction (k_y, green line). The nominal k-space evolution is plotted for comparison (black and black-dotted line): The only apparent difference is the reduced k_{max} of the measured compared to the prescribed k_x. (C) 2nd order phase coefficients: maximum phase in a spherical acquisition volume of 20 cm diameter. The concomitant field in $k_6 \propto 2z^2 - (x^2 + y^2)$ exhibits the strongest deviation to the spatial non-linearity of the phase evolution.

In turn, the distribution of these actual sampling points determines the realized acquisition density d_{acq}, whose resemblance to a Gaussian

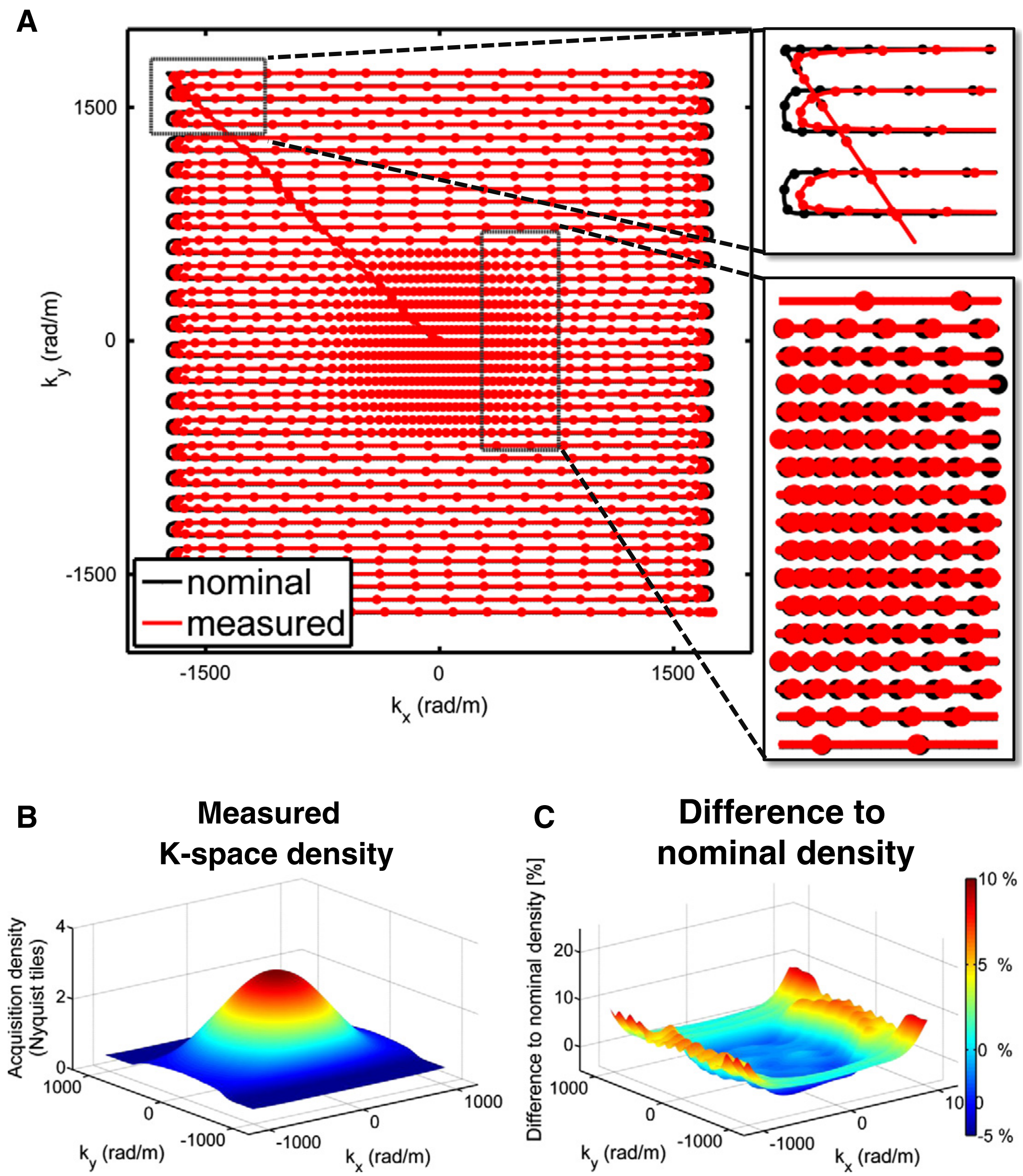

Fig. 4. Measured 2D sampling scheme and k-space acquisition densities of the matched-filter EPI trajectory. (A) 2D visualization of the measured (red) and nominal (black) trajectory. Dots indicate every 10th k-space sample. The general shapes of the nominal and measured trajectory, including the more densely sampled k-space center, coincide. However, the individual position of samples as well as the EPI turns differ between nominal and measured trajectory (zoomed insets). (B) k-space acquisition density calculated from the measured 2D trajectory. The shape approximates a Gaussian distribution. (C) Difference between k-space acquisition density of measured and nominal k-space trajectory. While the realized density in k-space center is slightly lower than prescribed (RMSE 3%), the actual EPI turns provide an increased density in k-space periphery (RMSE 20%).

is crucial for the expected SNR gains derived in the theory section of this paper. Visually, the 2D sampling point distribution (Fig. 4) indicates a density weighting with rotational symmetry which was assessed quantitatively using a gridding-based estimation of the acquisition density from the sampling points (Jackson et al., 1991). Indeed, the acquisition density is Gaussian (Fig. 4B), but, compared to the nominal density, exhibits a slight reduction (root mean square error, RMSE, 3%) in k-space center, i.e. for $|k| < 60\%\ k_{\max}$, and considerable overshoot (RMSE 20%) at its periphery, i.e. the EPI turns (Fig. 4C).

In summary, even though the individual positions of the k-space samples vary between nominal and actual trajectory, the induced densities exhibit high similarity and render the matched-filter prerequisites on the expected SNR gains valid.

Monitoring: Image reconstruction

Fig. 5 shows the unsmoothed reconstructed images of the undersampled, single-shot variable-density EPI acquisition in comparison to the spin-warp image acquired for coil sensitivity estimation. The matched-filter EPI (Fig. 5A) exhibits a low level of artifacts and high geometric congruency to the spin-warp image used as anatomical reference (Fig. 5C). Specifically, the edges of the brain, CSF and gray/white matter boundaries coincide in the matched-filter EPI and the anatomical reference (Fig. 5B, edges of spin-warp image overlayed on matched-filter EPI).

We investigated the particular impact of concurrent field monitoring on image quality in a series of alternative reconstructions, where we either used the nominal trajectory, the fully monitored 1st order trajectory

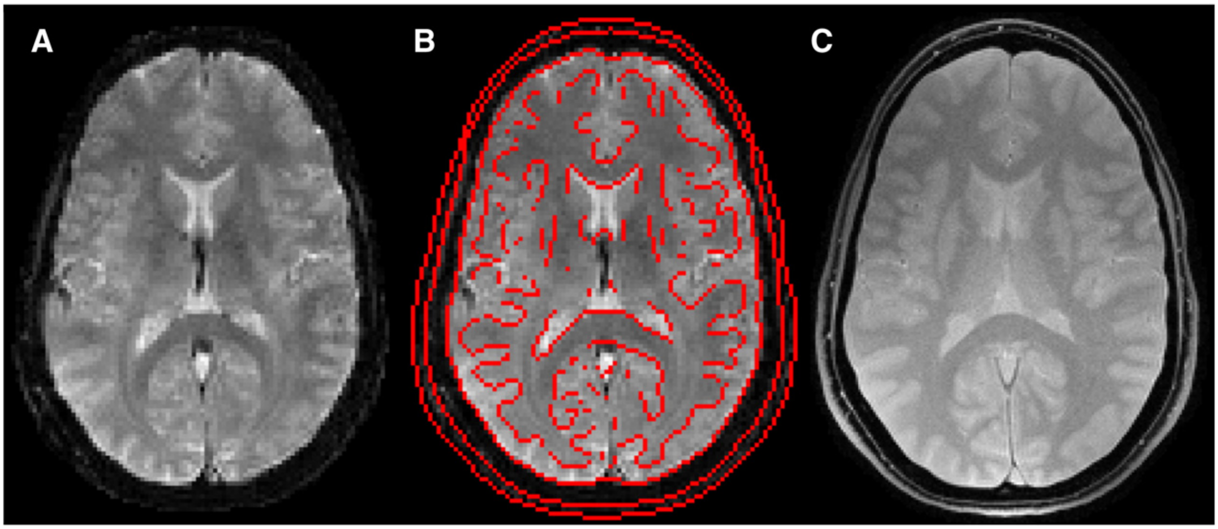

Fig. 5. Image quality and geometric accuracy of a single-shot matched-filter EPI slice reconstructed with concurrent field monitoring data, SENSE (3) and B_0-map based conjugate-phase correction. (A) Matched-filter EPI reconstruction, virtually artifact-free. (B) Geometric accuracy: An edge contour map of the geometric reference (C) overlaid onto (A). (C) Spin-warp image used as geometric reference and as 1st TE image for the B_0-correction.

including the global phase k_0, or a hybrid reconstruction with measured global phase, but nominal k_x and k_y, as input to the gridding-based iterative reconstruction (Fig. 6). The resulting images show the necessity of a reconstruction utilizing full knowledge about the actual trajectory and global phase. While this image reconstruction is virtually artifact-free, a reconstruction on the sole nominal trajectory exhibits both ghosting and blurring artifacts (Fig. 6B, D, G, I). The reconstruction incorporating the measured global phase to the nominal trajectory sheds light on the different artifact mechanisms (Fig. 6C, E, H, J): The ghosting edges parallel to phase encoding direction k_y are greatly reduced for this reconstruction, hence they mainly stem from a mismatch in k_0 during the readout. However, the blurred, rippled edges along frequency encoding direction remain and, thus, are presumably related to the gradient impulse response-induced compression of the matched-filter trajectory along k_x.

SFNR analysis

We evaluated local SFNR for each EPI session as a function of signal strength, which is proportional to the sine of the excitation flip angle (Fig. 7). First, we captured the statistics of pure thermal noise by measuring a session with 0° excitation flip angle, both in the phantom and in vivo (Fig. 7, horizontal dashed lines). Before reconstruction, each of these measured noise instances was added to the coil data of one fixed scan of the 90° session to evaluate pure thermal noise influence on SFNR. In this limiting case, the local SFNR gain of matched-filter compared to uniform EPI reached 45%, in good congruence with the theoretical expectation of 41%.

Secondly, in the phantom, the SFNR increased with signal level for both, matched-filter and uniform EPI, but with a steeper slope for matched-filter EPI, thus preserving an SFNR advantage compared to uniform EPI. However, the observed SFNR gain decreased for higher signal level (Fig. 7A, blue-shaded area). This indicates MR signal fluctuations in addition to thermal noise, which could occur at any stage of the excitation, encoding and reception process. Nevertheless, even for the practically relevant case of high signal level, the SFNR gain in the phantom remained well above 30% for matched-filter compared to uniform EPI.

Finally, for the in vivo measurements, we found regional differences in the SFNR dependence on signal level, most likely due to varying contributions of physiological noise in the areas considered: For white matter ROIs, the SFNR curves resembled those in the phantom, but exhibiting a lower minimal SFNR gain at high signal levels of about 20% for matched-filter compared to uniform EPI (Fig. 7B). In areas containing cerebro-spinal fluid (CSF), on the other hand, SFNR increased at low, but decreased at high signal level, presumably due to the strong pulsatile physiological noise (Fig. 7D; Krüger and Glover, 2001). However, we could still observe a relative gain in SFNR of about 15% for matched-filter compared to uniform EPI. For fMRI-relevant gray matter ROIs, an SFNR gain of up to 20% was found at high signal levels. The individual matched and uniform SFNR curves resembled those in white matter qualitatively, while the SFNR ratio exhibited decay with flip angle as in CSF, presumably reflecting the intermediate contribution of physiological noise in gray matter regions compared to white matter and CSF (Fig. 7C).

fMRI analysis: t-maps and total least squares

In the individual SPM analysis of each acquired session, all contrast maps showed the expected activations patterns, representing the quarter-fields in the visual cortex by contrasting the two stimulation blocks either as ULLR–URLL (contrast 1, Fig. 8, red voxels) or URLL–ULLR (contrast 2, Fig. 8, green voxels). The activation patterns are visualized as overlays on an EPI scan of the corresponding session and show nice alignment with gray matter structures in the individual subject. Comparing the t-maps in terms of peak t-values and cluster sizes of significant voxels, the sessions with matched-filter acquisitions outperformed uniform EPI acquisitions consistently within subjects (across sessions) and between subjects (Fig. 8, Table 2). In particular,

Fig. 6. Image reconstructions of matched-filter EPIs using nominal and concurrently monitored field evolutions. (A–E) Uniform EPI, (F–J) Matched-filter EPI. (A, F) Coil data reconstructed with the concurrently monitored k_0-phase and linear k-space trajectory. (B, G) Reconstruction with nominal k-space trajectory. (C, H) Hybrid reconstruction with nominal k-space trajectory, but incorporating the measured k_0-phase.(D) Difference image of (B) and (A): The mismatch to the actual trajectory creates prominent SENSE-ghosting in phase encoding direction as well as strong intensity modulations. Artifact levels reach up to ± 20 % voxel intensity. (E) Difference image of (C) and (A). Correcting for the measured k_0-phase, but reconstructing on the nominal trajectory greatly reduces intensity modulations, but does not fully eliminate image artifacts due to SENSE-ghosting.(I) Difference image of (G) and (F): The mismatch to the actual trajectory creates prominent SENSE-ghosting in phase encoding direction as well as Gibbs-like ringing artifacts close to tissue edges in readout direction. Artifact levels reach up to ± 20 % voxel intensity. (J) Difference image of (H) and (F). Correcting for the measured k_0-phase, but reconstructing on the nominal trajectory greatly reduces image artifacts due to SENSE-ghosting, while the edge-ringing and blurring artifacts remain unaltered.

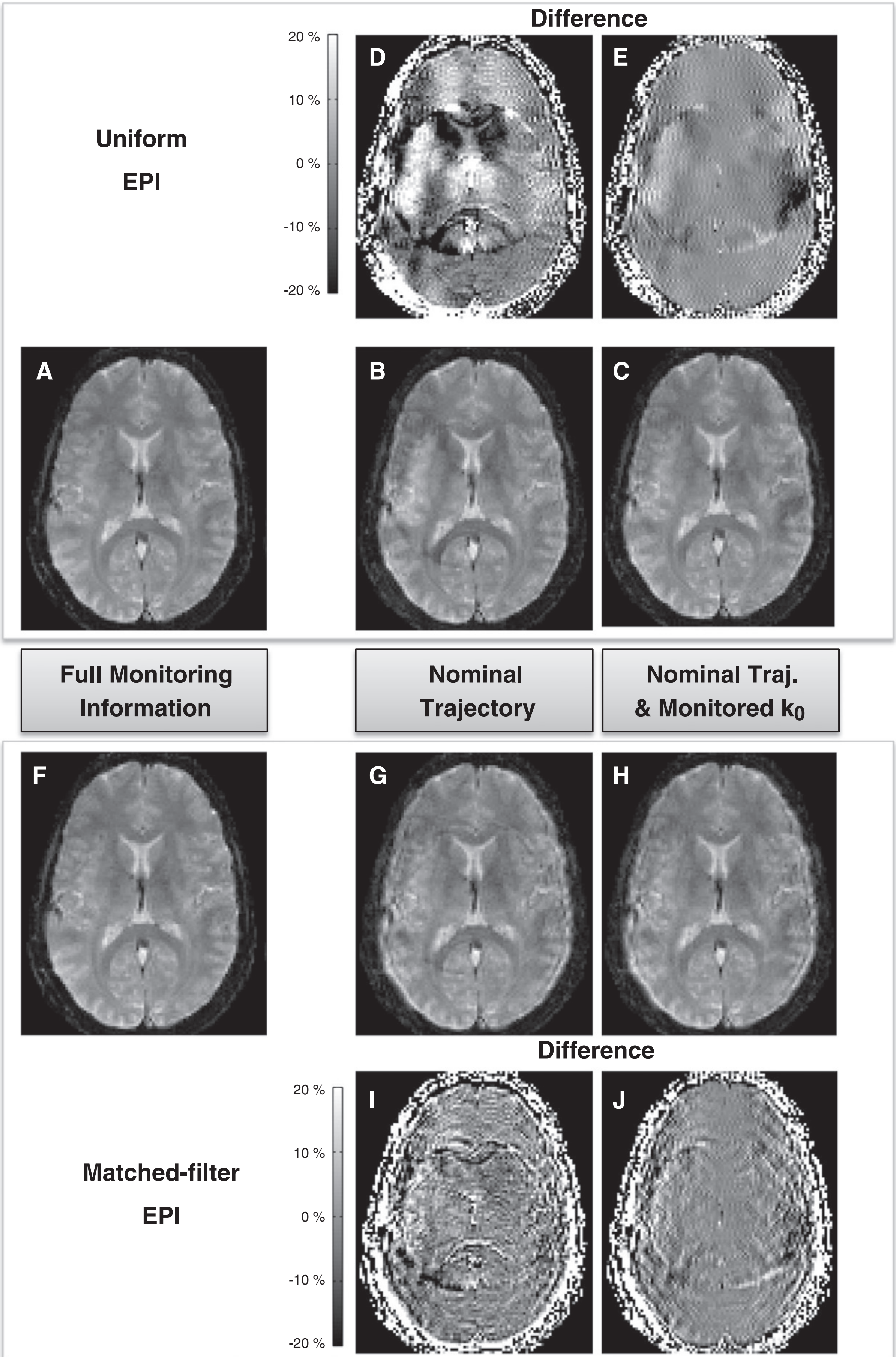

Difference
20 %
10 %
0 %
-10 %
-20 %
D
E
Uniform
EPI
A
B
C
Full Monitoring
Information
Nominal
Trajectory
Nominal Traj.
& Monitored k0
F
G
H
Difference
20 %
10 %
0 %
-10 %
-20 %
I
J
Matched-filter
EPI

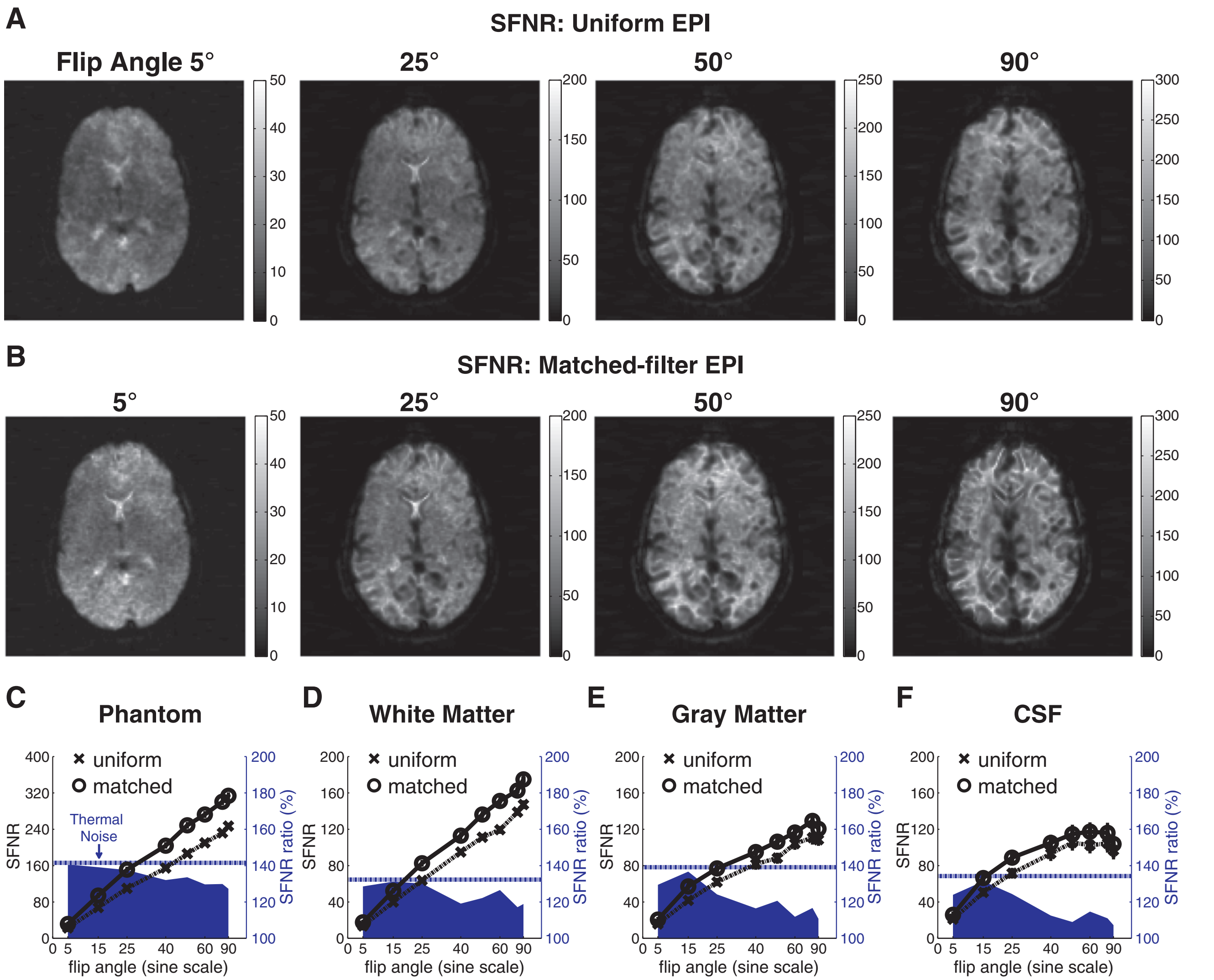

Fig. 7. Dependence of matched-filter signal-to-fluctuation-noise-ratio (SFNR) advantage on signal level (sine of excitation flip-angle). (A) In vivo resting-state SFNR maps for uniform EPI scans after smoothing. For low signal levels (5°–25 °), the SFNR distribution is governed by the SENSE geometry factor and mean signal level. For medium and high signal levels (50°–90°), the contrast is increasingly dominated by physiological noise prevalence. (B) In vivo resting-state SFNR maps for matched-filer EPI scans after smoothing. For all signal levels, SFNR is increased compared to the uniform EPI SFNR maps in (A). The delineation of regions with different physiological noise prevalence is even more pronounced than in uniform EPI (cf. white matter in 90° SFNR map). (C) Phantom data: Approximately linear SFNR increase for uniform and matched-filter EPI (black curves; standard error of the mean smaller than dot size). The ratio of SFNR (blue shade) between matched-filter and uniform EPI drops below the SFNR gain bound determined by pure thermal noise (dotted horizontal line) for high signal levels. (D) In vivo resting-state SFNR for a brain region containing white matter. The SFNR dependence on signal level resembles the phantom data in (C). (E) In vivo resting-state SFNR for a gray matter brain region. Compared to white matter (D), the SFNR gains for high signal levels become more variable. (F) In vivo resting-state SFNR for a brain region containing cerebro-spinal fluid (CSF): Contrary to white and gray matter, SFNR drops in CSF for high signal levels. Still, a considerable SFNR gain advantage of matched-filter compared to uniform EPI acquisition remains.

for both the first and second repetition (effect of session) of each acquisition in all subjects, matched-filter EPI provided superior activation patterns (according to the aforementioned criteria) than uniform EPI, whereas the activation patterns within an acquisition modality resembled each other in the 1st and 2nd repetition.

For a more quantitative and comprehensive view on this improved BOLD contrast sensitivity, especially its robustness and test/retest reliability, we generated a scatter plot depicting each individual voxel of a subject (Fig. 9). The *t*-value change in the session of interest was plotted against the original *t*-value of the corresponding voxel in the reference session. Significant voxels were colored with the colors of the corresponding contrasts. As contrast 2 was just the negative of contrast 1, the voxels with highly negative *t*-values for contrast 1 ($t < -4.73$, corresponding to a peak level family-wise error correction at $p = 0.05$) were significant voxels in contrast 2.

This data representation was evaluated using a total least squares (TLS) estimation of the mean slope $\Delta t/t$, which indicates the relative increase in contrast (and therefore BOLD) sensitivity for the session of interest compared to the reference session, averaged over all voxels significant in both sessions (Table 3). TLS is an extension of ordinary least squares regression for cases where both dependent and independent variables contain observation noise, as in our case.

At the single-subject level, performing TLS between matched-filter and uniform EPI sessions assessed the average effect of the acquisition scheme on BOLD sensitivity (Fig. 9A, B), while TLS between session 1 and 2 of the same acquisition scheme (uniform or matched) provided a measure of test–retest reliability (Fig. 9C, D), with a horizontal line indicating identical replication. For example, in the most consistent data set (subject 4, Fig. 9A–D), the TLS analyses comparing matched and uniform acquisition yielded a positive slope indicating a *t*-value increase of 35% ± 2% (95% confidence limits using bootstrapping) in session 1 (Fig. 9A) and 41% ± 2% in session 2 (Fig. 9B). At the same time, the TLS analyses comparing sessions 1 and 2 found high test–retest reliability within each acquisition scheme, with session differences of only

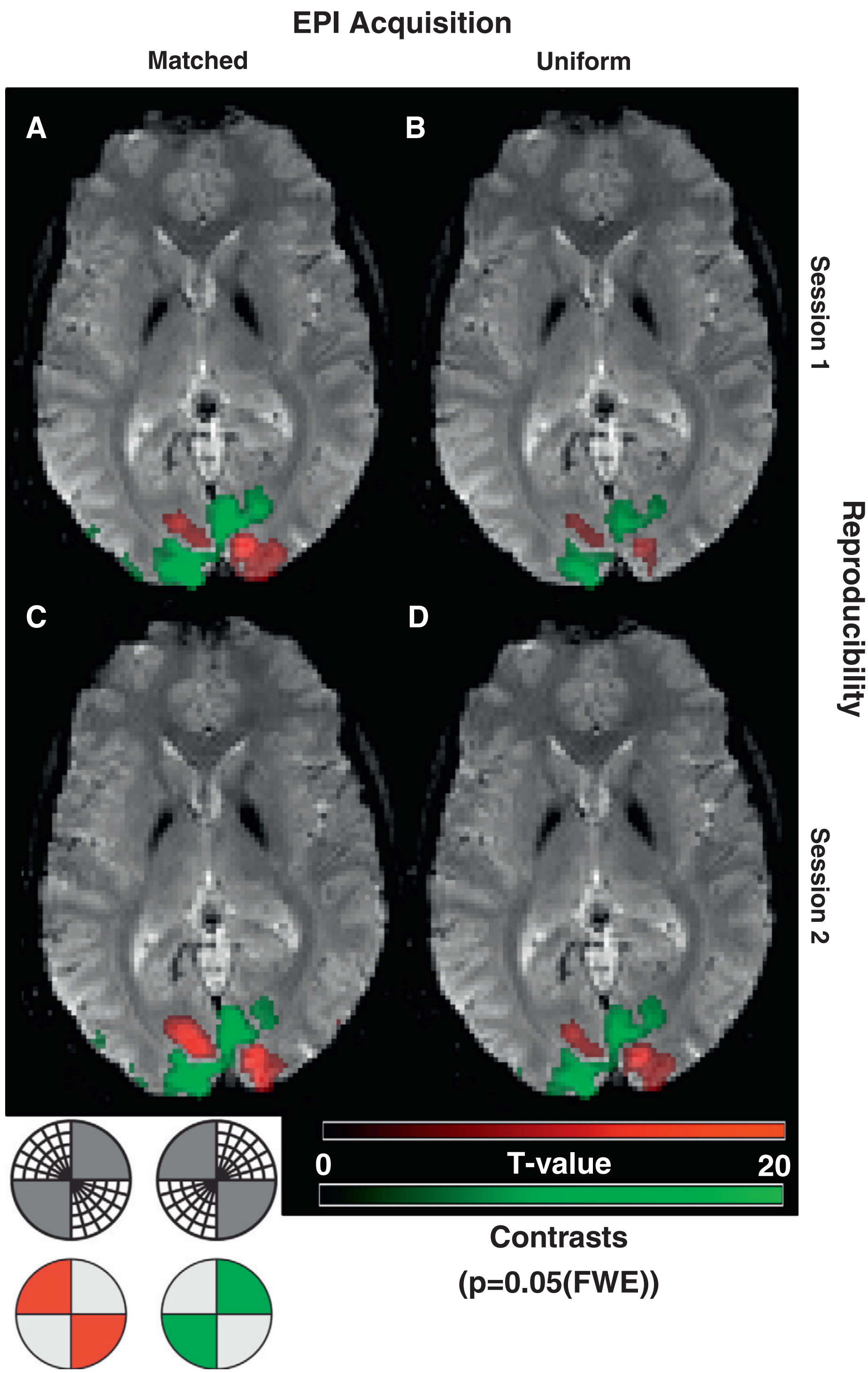

Fig. 8. Single-subject activation patterns for task fMRI sessions utilizing a visual quarter-field stimulation. Depicted are the t-maps (FWE-corrected $p = 0.05$ peak level) for the differential contrast of condition 1 vs. 2 (red colormap) and 2 vs. 1 (green colormap), overlayed on the mean EPI image of the corresponding sessions. The topological organization of the early visual areas is clearly recovered by the activation patterns. For the 1st as well as the 2nd repetition of the fMRI sessions, cluster extent and peak level t-value were significantly increased in both contrasts for the matched-filter EPI compared to the uniform acquisition. (A) Matched-filter EPI, 1st session. (B) Uniform EPI, 1st session. (C) Matched-filter EPI, 2nd session. (D) Uniform EPI, 2nd session.

2% ± 1% and 7% ± 2% for the matched-filter and uniform acquisition, respectively (Fig. 9C, D).

The average effect of the acquisition scheme on BOLD sensitivity was consistently found in all other subjects as well: TLS yielded exclusively positive slopes when comparing matched to uniform sessions (Table 3), with the average t-value gain ranging from 14% to 146%. The magnitude of this t-value gain typically corresponded to the increase in cluster extent and/or peak t-value of significant voxels (Table 2). However, two subjects (1 and 3) exhibited poor test–retest reliability in TLS analyses between sessions 1 and 2 within each acquisition scheme, presumably due to bulk motion and subsequent voxel mis-registration, that might explain the unexpectedly high sensitivity gains of 83% ± 3% and 146% ± 19%. Nevertheless, even for these subjects, matched-filter acquisition consistently showed higher peak level

Table 2
Peak-statistic and voxel count per subject for significant activation after peak level family-wise error correction ($p = 0.05$ FWE) in both relevant functional contrasts. The sessions matched 1 and uniform 1 were measured back to back, followed by uniform 2 and matched 2. The order of matched and uniform acquisition was counter-balanced between subjects and independently for first and second repetition. (Left) Contrast 1: Upper left lower right (ULLR)–Upper right lower left (URLL) checkerboard wedges. (Right) Contrast 2: URLL–ULLR.

Subject	Peak *t*-value and number of activated voxels (contrast 1)			
	Uniform 1	Uniform 2	Matched 1	Matched 2
1	17.7	11.8	16.6	11.7
2	21.2	19.7	22.7	19.7
3	11.8	17.1	20.7	29.5
4	23.0	22.0	29.5	29.1
Subject	**Peak *t*-value and number of activated voxels (contrast 2)**			
	Uniform 1	Uniform 2	Matched 1	Matched 2
1	18.2	10.2	22.8	21.6
2	19.7	20.1	22.6	24.6
3	11.9	15.6	21.0	19.8
4	20.0	18.1	27.2	23.9

and/or larger cluster extents compared to the uniform session measured back-to-back, i.e. matched 1 vs. uniform 1 and matched 2 vs. uniform 2 (Table 2).

At the group level, a pooled TLS analysis comprising all significant voxels of all subjects and sessions yielded an average *t*-value gain of 37% for matched-filter compared to uniform EPI acquisitions of corresponding sessions (Fig. 9E). This main effect of acquisition scheme was also significant in a two-way (acquisition by session) repeated measures analysis of variance (ANOVA) of the TLS slopes (Table 3) normalized to uniform session 1 ($F(1, 3) = 14.0$, $p < 0.05$). No main effect of session or interaction between acquisition and session could be found ($F(1, 3) = 0.37$, $p > 0.58$; $F(1,3) = 0.46$, $p > 0.54$). Due to the small number of measurements, we also performed a non-parametric test on the TLS slopes that confirmed the main effect of acquisition, with matched > uniform directionality (Mann–Whitney $U = 58$, $n_1 = n_2 = 8$, $p < 0.005$ one-tailed; implementation: http://vassarstats.net).

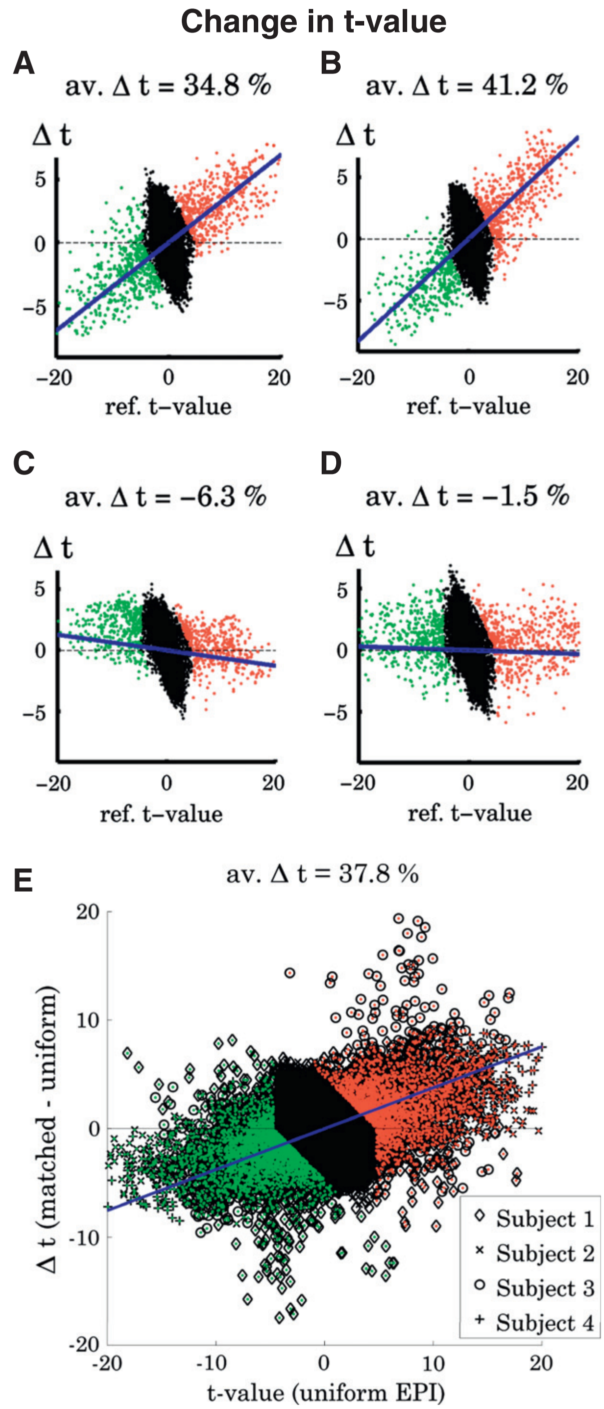

Fig. 9. Whole-brain summary of BOLD sensitivity gains and reproducibility for matched-filter compared to uniform EPI acquisition. Scatter plots depict all significant voxels, plotting the *t*-value change in a session of interest compared to a reference session against the *t*-value in that reference session. Significant voxels for contrasts 1 and 2 are colored in red and green, respectively. A total least squares (TLS) fit summarizes the *t*-value change over all voxels. (A–D) Single-subject (no. 4) scatter plots and TLS fits. Effect of acquisition scheme (matched vs. uniform): (A) session 1; (B) session 2. Strength of reproducibility (session 2 vs. session 1): (C) uniform EPI; (D) matched-filter EPI. (E) Group level scatter plot and TLS fit pooling significant voxels of all subjects and sessions, comparing matched to uniform acquisition (pairing matched 1 to uniform 1 and matched 2 to uniform 2).

Discussion and conclusion

The results presented have shown the feasibility of a matched-filter acquisition for fMRI in four stages: First, we verified that a single-shot EPI trajectory with Gaussian acquisition density and typical resolution and readout duration can be accomplished within the limits of a commercial MR gradient system. The concurrent field monitoring results confirmed that the experimentally realized acquisition density was indeed Gaussian, as is optimal for the Gaussian filter post-processing, with a root mean squared error (compared to the prescribed Gaussian density) of 3% in k-space center and 20% at the EPI turns.

Secondly, virtually artifact-free image reconstructions could be retrieved from these matched-filter k-space trajectories. To this end, it was crucial to perform image reconstructions using both static B_0-field correction as well as concurrent dynamic field monitoring for highest image quality. Concurrent field monitoring proved to be a robust and reliable method for correcting eddy-current and gradient imperfections. In this study, effects on 0^{th} and 1^{st} order phase coefficients entered our image reconstruction (although extensions to incorporate concurrently monitored higher-order phase information exist; Wilm et al., 2011, 2012). Alternatively, reproducible deviations from the nominal k-space trajectory could be corrected using a calibration-based image reconstruction method (Graedel et al., 2013) that relies on the characterization of the gradient impulse response function in an independent, field monitoring-based experiment (Vannesjo et al., 2013a,b).

Thirdly, we have seen that the experimentally obtained SFNR improvements in the phantom and in vivo match the theoretically derived SFNR gains of 40% very well in the regime of thermal noise. Furthermore, even in the regime of high signal-induced noise contributions, a substantial SFNR increase of about 20% could be retained. Last, and most importantly, these SFNR increases translated into improved sensitivity for task-based fMRI contrasts, as demonstrated

Table 3
BOLD sensitivity increase in task-based fMRI using matched-filter acquisition. The mean *t*-value increase (including 95% confidence limits determined by bootstrapping) is reported, as computed by the TLS analysis for the relevant contrasts, comparing all pairs of sessions (columns) for all subjects (rows). A graphical representation of the corresponding data is depicted in Fig. 9, in particular all four pair-wise session comparisons of subject 4 (Fig. 9A–D).

Subject	Mean percent *t*-value change and 95% confidence limits			
	Session 1 matched vs. uniform	Session 2 matched vs. uniform	Uniform session 2 vs. session 1	Matched session 2 vs. session 1
1	39.7 (7.4)	145.6 (18.9)	−46.2 (2.1)	−21.5 (3.0)
2	23.7 (1.3)	14.7 (1.5)	11.9 (1.3)	2.2 (1.6)
3	83.1 (2.4)	42.7 (4.2)	80.3 (4.4)	30.4 (4.4)
4	34.8 (1.3)	41.2 (1.4)	−6.3 (1.1)	−1.5 (1.0)

by a comparison of voxel-wise *t*-statistics under matched-filter and uniform EPI acquisition. A total least squares analysis for *t*-values of corresponding voxels confirmed that *t*-statistics of significant voxels were replicably higher for matched-filter fMRI by 20–40%. On top of that, again using TLS, we confirmed that in most subjects this difference was considerably higher than the within-modality *t*-value fluctuations of matched-filter and uniform EPI acquisition sessions, though the small number of subjects precludes a generalization of these preliminary findings.

In summary, it is remarkable that despite the multiple potential image artifact mechanisms and limited scope of our theoretical noise considerations, a considerable portion of the theoretical SNR advantage of matched-filter fMRI could be preserved through these four stages. Still, the quantitative progression of the realized SFNR gains within and through these stages deserves further discussion here, most prominently (1) the decrease of the in vivo SFNR gain from 40% to 20% for high signal levels, and (2) the subsequent rise of contrast-to-noise ratio (CNR) advantage in task-based fMRI to 20–40% compared to the aforementioned 20% SFNR increase in resting-state. Both observations arise from the intricate noise situation for in vivo time series, which violates the white Gaussian noise assumption exploited in our theoretical treatment of matched-filter acquisitions. These deviations from a flat noise spectrum are induced by fluctuations in the measured MR signal and can be categorized into two classes: system-dependent and object-dependent fluctuations.

Typically, object-dependent fluctuations are the dominant non-white noise source in MRI, particularly at high main field strength (Krüger and Glover, 2001; Triantafyllou et al., 2006). They arise from the measured physiological systems themselves, which frequently exhibit a tendency towards low frequency noise, i.e. a "pink" noise spectrum, e.g. through breathing and cardiac pulsation (Birn et al., 2008; Chang et al., 2009; Dagli et al., 1999; Glover et al., 2000; Shmueli et al., 2007). System-dependent MR signal fluctuations, on the other hand, were particularly small in our measurements, since the concurrent field-monitoring approach corrected for instabilities in the encoding main and gradient fields, as well as any clock jitter of the spectrometer. Still, non-white noise components might have been introduced in the transmission and reception chain of the system, i.e. the excitation B_1 field and receiver gain, respectively.

A general quantification of these system- and object-dependent noise spectra is challenging, but may in principle serve two applications. Firstly, the prediction of in vivo matched-filter SFNR gains could become more accurate when deduced from a pink noise spectrum. Specifically, the upper bound on SFNR gain computed in the theory section for white noise would become tighter, because acquisition weighting unfolds its full strength if noise adds up incoherently, i.e. for white noise. In principle, these pink noise assumptions could then predict the aforementioned deviation between low and high signal level SFNR gain in our resting-state experiments.

Secondly, one could envisage a pink noise spectrum dictating different acquisition strategies to achieve the maximum SFNR gain. However, pink noise shares spectral characteristics with the BOLD signal of interest, thus accruing with similar coherence over time. Consequently, both pink noise *and* BOLD signal might be suppressed by an acquisition matched in this way, causing information loss. For pink noise, it therefore seems preferable to rely not only on noise statistics, but rather the exact knowledge of the occurring noise instances. Actual instances of physiological noise, for example, can be readily modeled from peripheral measures, such as ECG and breathing belts, and used as confound regressors to de-noise voxel time series, e.g. using RETROICOR (Glover et al., 2000; Hutton et al., 2011; Kasper et al., 2009). The second quantitative deviation in our experiments (up to 40% CNR increase for task-based fMRI compared to only 20% SFNR increase in "resting-state" fMRI) may be understood as a special case of this pink noise correction: While spontaneous BOLD fluctuations in resting-state were considered "noise", thus lowering the SFNR, the contrast-related BOLD responses in significant voxels were identified as signal of interest and therefore did not contribute to the residual error, i.e. noise amplitude, for the task-based fMRI sessions. Consequently, also resting-state connectivity analysis (Biswal et al., 1995), in contrast to pure SFNR measurements, should benefit from matched-filter acquisition on the same order as task-based fMRI, because correlations in (BOLD) signal fluctuations become a signal of interest here. Hence, the confounding noise in correlation detection has a noise spectrum more similar to white noise and the matched-filter theory assumptions.

In this work, we exemplified the principle of matched-filter acquisition, showing how a variable density 2D EPI readout can be used in fMRI to achieve SNR optimality for a Gaussian target PSF. The general framework of matched-filter acquisition, however, is not restricted to any of the four design decisions made here; neither the EPI readout, nor the Gaussian target PSF, not the fMRI application and not even the criterion of SNR optimality. In the following, we will conclude with an outlook to possible extensions of matched-filter acquisitions regarding these four aspects, in order of increasing generality:

Choosing a 2D EPI trajectory to implement a variable density acquisition was motivated by demonstrating the matched-filter principle for the currently most robust and commonly used readout in fMRI. However, as shown in Eq. (10), the SFNR gain scales with the square root of covered k-space volume, which promises an even greater advantage for 3D matched-filter acquisitions, such as concentric shell trajectories (Zahneisen et al., 2012) or the 3D EPIs recently adopted for fMRI (Lutti et al., 2013; Poser et al., 2010). More generally, the choice of the EPI trajectory itself for a Gaussian smoothing kernel is suboptimal. Inevitably, the EPI turns at traverse ends waste acquisition time in the de-emphasized high-frequency regime of the target PSF. Spiral readouts (Ahn et al., 1986; Glover and Lai, 1998) might be natural alternatives to implement a Gaussian acquisition density, since they are rotationally symmetric, and have been successfully utilized for variable density acquisitions before (Chang and Glover, 2011). Moreover, they feature only a few sharp turns in the k-space center, thus allowing for more efficiency in realizing the prescribed acquisition density. However, their sensitivity to static B_0 inhomogeneity poses a considerable challenge (Börnert et al., 1999).

The next design consideration refers to the selection of a Gaussian target PSF itself: While smoothing with a Gaussian kernel is prevalent, other filters for image post-processing in fMRI applications have been proposed, such as prolate spheroidal functions or wavelets (Lindquist and Wager, 2008; Van De Ville et al., 2006; Yang et al., 2002). The rationale for matched-filter acquisition holds unaltered for any target PSF, as do the global SNR gains derived in Eq. (10), as long as the target PSF is shift-invariant. For more specialized applications, e.g. cortical surface mapping or adaptive smoothing (Andrade et al., 2001; Harrison et al., 2008; Tabelow et al., 2006), taking into account regional anatomical variability for kernel adaptation, a matched-filter acquisition strategy will achieve SNR optimality for one pre-selected kernel, i.e. only locally in the image.

Beyond fMRI, fast single-shot readouts using matched-filter acquisitions may have applications in other notoriously low-SNR measurements such as echo-planar spectroscopic imaging (EPSI), diffusion- or perfusion-weighted imaging. Here, other target PSFs, such as Hamming filters for ringing suppression, might be desirable (Greiser et al., 2005; Kasper et al., 2012; Stobbe and Beaulieu, 2008). However, enforcing density weighting via gradient modulation for an arbitrary target PSF requires a more general method to design the gradient waveform than the one presented here for the Gaussian PSF. To this end, a promising algorithm for time-optimal gradient waveform design was presented by (Lustig et al., 2008), which could be extended to allow for variable k-space densities through arc-length parameterized gradient limits along the trajectory, hence implementing Eq. (11).

One limitation of our approach to achieve acquisition density weighting with a variable velocity in k-space is the requirement of sufficient flexibility for gradient modulation. Therefore, readouts that require maximum gradient amplitude or slew rate at all times cannot be augmented by a matched-filter acquisition. Objectives like robustness to T^*_2 and off-resonance effects, ultra-high spatial resolution or large slice coverage demand these maximally fast readouts. Alternatively, in these cases, a partial matched-filter acquisition weighting can be achieved in phase encoding direction by varying phase blip gradient moments, i.e. spacing of k-space traverses (Kasper et al., 2010; Zeller et al., 2013). Such variable spacing of k-space lines typically violates Nyquist sampling and thus necessitates parallel imaging or additional k-space traverses at the expense of lower acquisition efficiency (due to additional traverse turns). Inherently, it can only achieve filter-matching in phase encoding direction, limiting the expected SNR increase to the square root of the 2D matched-filter acquisition through velocity variation as presented here. Moreover, recent advances in gradient performance that allow for maximum gradient strengths of 100–300 mT/m and slew rates above 200 T/m/s (Kimmlingen et al., 2012; Van Essen et al., 2012), might lift current constraints on velocity-modulated matched-filter acquisition in the near future to open up its versatility and application range even further.

On a final, conceptual note, SNR optimality is only one, albeit important, criterion for coordinating acquisition and reconstruction to shape signal and noise behavior. According to our Eq. (3), acquisition weighting can be recruited to design any noise variance landscape in k-space for a given target PSF, as the final noise variance in k-space is simply the ratio of the squared target PSF and acquisition density at each k-space position. For example, setting the acquisition density to a multiple of the squared target PSF, the dependence on k between numerator and denominator in Eq. (3) cancels out. Hence, the final noise variance in k-space is constant, i.e. flat, and, by the Fourier autocorrelation theorem, the noise variances in image space are uncorrelated. Taken together, this means that we can achieve voxel-wise noise decorrelation in an MR image by making the acquisition density proportional to the *square* of the target PSF. In this way, acquisition density matching could broaden its scope to areas where the delineation of unique signal contributions per voxel is crucial, such as high-resolution, layer-specific fMRI (Goense et al., 2012; Koopmans et al., 2010) and multivariate statistical analyses of fMRI data (Haynes and Rees, 2006), or applications that rely on voxel correlation measures, e.g. "resting-state" functional connectivity (Biswal et al., 1995; Buckner et al., 2013; Cole et al., 2010).

Acknowledgments

We would like to thank Chloe Hutton for a first version of the RETROICOR code and Jakob Heinzle for the contrast schematic in Fig. 8. Furthermore, we enjoyed helpful discussions with Christian Windischberger and Robert Turner concerning k-space densities and the BOLD HRF. Technical support from Philips Healthcare is gratefully acknowledged. This work was supported by grants from CTI (grant number 13756.1 PFFLM-NM) and NCCBI.

Appendix A

We calculate the expected SNR gain for a Gaussian smoothing kernel with a FWHM defining a k-space target density:

$$d_{\text{target}}(\boldsymbol{k}) = \begin{cases} C \cdot \exp\left(-\dfrac{\boldsymbol{k}^2\sigma_r^2}{2}\right) & \text{for } |\boldsymbol{k}| \leq k_{\max} \\ 0 & \text{otherwise} \end{cases} \tag{A.1}$$

with $k_{\max} = \frac{\pi}{\Delta x}$ and $\sigma_r = \text{FWHM}/\sqrt{8\ln 2}$ and $C = \text{const.}$, such that $\int_{V_k} d_{\text{target}}(\boldsymbol{k})\mathrm{d}\boldsymbol{k} = 1$.

As the Gaussian kernel is separable, we can calculate the SNR gain for each acquisition dimension individually utilizing Eq. (10), where $V_k = 2 \cdot k_{\max}$, and yield, for a d-dimensional scan:

$$\frac{\text{SNR}_{\text{matched}}}{\text{SNR}_{\text{uni}}} = \left(2 \cdot k_{\max} \cdot \int_{-k_{\max}}^{k_{\max}} d^2_{\text{target}}(k)\,\mathrm{d}k\right)^{\frac{d}{2}}. \tag{A.2}$$

The integral on the right-hand side can be expressed using the error function $\text{erf}(x) = \frac{1}{\sqrt{\pi}}\int_{-x}^{x} e^{-k^2}\mathrm{d}k$ via variable substitution $k \to k\sigma_r$ yielding

$$\frac{\text{SNR}_{\text{matched}}}{\text{SNR}_{\text{uni}}} = \left(2 \cdot k_{\max} \cdot C \cdot \frac{\sqrt{\pi} \cdot \text{erf}(k_{\max}\sigma_r)}{\sigma_r}\right)^{\frac{d}{2}}. \tag{A.3}$$

Because of $\int_{-k_{max}}^{k_{max}} d_{\text{target}}(k)\,\mathrm{d}k = 1$, C itself can be expressed via the error function as $C^{-1} = \frac{\sqrt{2\pi}\cdot\text{erf}\left(k_{\max}\sigma_r/\sqrt{2}\right)}{\sigma_r}$ to arrive at the final expression for the SNR gain using a matched-filter compared to a uniform acquisition:

$$\begin{aligned} \frac{\text{SNR}_{\text{matched}}}{\text{SNR}_{\text{uni}}} &= \left(2 \cdot k_{\max} \cdot \frac{\sigma_r}{\sqrt{2\pi} \cdot \text{erf}\left(k_{\max}\sigma_r/\sqrt{2}\right)} \cdot \frac{\sqrt{\pi} \cdot \text{erf}(k_{\max}\sigma_r)}{\sigma_r}\right)^{\frac{d}{2}} \\ &= \left(\sqrt{2} \cdot k_{\max} \cdot \frac{\text{erf}(k_{\max}\sigma_r)}{\text{erf}\left(k_{\max}\sigma_r/\sqrt{2}\right)}\right)^{\frac{d}{2}}. \end{aligned} \tag{A.4}$$

Appendix B

We derive the readout gradient time course $G(t)$ realizing a Gaussian acquisition density $d_{\text{acq}}(\boldsymbol{k})$ on a k-space traverse from $-k_{\max}$ to $k_{\max}$ as follows: By inserting the Gaussian target density of Eq. (A.1) into the differential Eq. (11), we first yield a concrete differential equation for the one-dimensional readout trajectory time course $k(t) := k_x(t)$:

$$|\dot{k}| = \frac{1}{d_{\text{acq}}(k)} = \widetilde{C} \cdot \exp\left(+\frac{k^2\sigma_r^2}{2}\right) \tag{B.1}$$

where tilded C refers to a constant of no interest.

As k should increase monotonously during a traverse, $\dot{k} \geq 0$ and we can neglect the absolute value in Eq. (B.1). Following a logarithmic transform and differentiation, Eq. (B.1) appears in the normal form of a second order non-linear ordinary differential equation

$$\ln k - \frac{\sigma_r^2}{2} k^2 = \tilde{\tilde{C}} \overset{\frac{d}{dt}}{\Rightarrow} \frac{\ddot{k}}{\dot{k}} - \sigma_r^2 k\dot{k} = 0 \qquad \Rightarrow \ddot{k} - \sigma_r^2 \dot{k}^2 \cdot k = 0. \tag{B.2}$$

The general solution for this differential equation reads

$$k(t) = \frac{\sqrt{2}}{\sigma_r} \cdot \mathrm{erf}^{-1}\left(\sqrt{\frac{2}{\pi}} c_1 \sigma_r (t + c_2)\right) \tag{B.3}$$

with erf^{-1} being the inverse error function and $c_{1,2}$ constants to be determined via side conditions.

The side conditions arise as the interval $-k_{\max}$ to $k_{\max}$ has to be covered within a traverse duration T_{traverse}, i.e.

$$k(0) = -k_{\max} \Rightarrow -\sqrt{\frac{\pi}{2}} \cdot \frac{1}{\sigma_r} \cdot \mathrm{erf}\left(\frac{\sigma_r k_{\max}}{\sqrt{2}}\right) = c_1 c_2 \tag{B.4}$$

$$k(T_{\text{traverse}}) = k_{\max} \Rightarrow \sqrt{\frac{\pi}{2}} \cdot \frac{1}{\sigma_r} \cdot \mathrm{erf}\left(\frac{\sigma_r k_{\max}}{\sqrt{2}}\right) = c_1 (T_{\text{traverse}} + c_2). \tag{B.5}$$

Dividing Eq. (B.5) through Eq. (B.4) and back-substitution into Eq. (B.4) provides the values for $c_{1,2}$ as

$$-1 = \frac{T_{\text{traverse}} + c_2}{c_2} \Rightarrow c_2 = -\frac{T_{\text{traverse}}}{2} \tag{B.6}$$

$$c_1 = \frac{\sqrt{2\pi}}{T_{\text{traverse}} \sigma_r} \cdot \mathrm{erf}\left(\frac{\sigma_r k_{\max}}{\sqrt{2}}\right). \tag{B.7}$$

From that, we yield the final form for the k-space trajectory evolution as

$$k(t) = \frac{\sqrt{2}}{\sigma_r} \cdot \mathrm{erf}^{-1}\left(\mathrm{erf}\left(\frac{\sigma_r k_{\max}}{\sqrt{2}}\right) \cdot \left(2\frac{t}{T_{\text{traverse}}} - 1\right)\right). \tag{B.8}$$

Taking the temporal derivative of Eq. (B.8), we yield the gradient waveform as specified in Eq. (12):

$$G(t) = \frac{\dot{k}(t)}{\gamma} = \underbrace{\frac{\sqrt{2\pi} \cdot \mathrm{erf}\left(\frac{\sigma_r k_{\max}}{\sqrt{2}}\right)}{\gamma T_{\text{traverse}} \sigma_r}}_{C_1} \exp\left(\mathrm{erf}^{-1}\left(\underbrace{\mathrm{erf}\left(\frac{\sigma_r k_{\max}}{\sqrt{2}}\right)}_{C_2} \cdot \left(2\frac{t}{T_{\text{traverse}}} - 1\right)\right)\right)^2. \tag{B.9}$$

References

Ahn, C.B., Kim, J.H., Cho, Z.H., 1986. High-speed spiral-scan echo planar NMR imaging-I. IEEE Trans. Med. Imaging 5, 2–7. http://dx.doi.org/10.1109/TMI.1986.4307732.

Andrade, A., Kherif, F., Mangin, J.-F., Worsley, K.J., Paradis, A.-L., Simon, O., Dehaene, S., Le Bihan, D., Poline, J.-B., 2001. Detection of fMRI activation using cortical surface mapping. Hum. Brain Mapp. 12, 79–93. http://dx.doi.org/10.1002/1097-0193(200102)12:2<79::AID-HBM1005>3.0.CO;2-I.

Barmet, C., De Zanche, N., Pruessmann, K.P., 2008. Spatiotemporal magnetic field monitoring for MR. Magn. Reson. Med. 60, 187–197.

Barmet, C., De Zanche, N., Wilm, B.J., Pruessmann, K.P., 2009. A transmit/receive system for magnetic field monitoring of in vivo MRI. Magn. Reson. Med. 62, 269–276. http://dx.doi.org/10.1002/mrm.21996.

Barmet, C., Wilm, B.J., Pavan, M., Katsikatsos, G., Keupp, J., Mens, G., Pruessmann, K.P., 2010. Concurrent higher-order field monitoring for routine head MRI: an integrated heteronuclear setup. Presented at the ISMRM, Stockholm. Proc. Intl. Soc. Mag. Reson. Med., 18, p. 216.

Barmet, C., Wilm, B.J., Kasper, L., Ruff, C.C., Stephan, K.E., Pruessmann, K.P., 2011. fMRI with concurrent magnetic field monitoring. Presented at the ISMRM, Montreal. Proc. Intl. Soc. Mag. Reson. Med., 19, p. 3609.

Beatty, P.J., Nishimura, D.G., Pauly, J.M., 2005. Rapid gridding reconstruction with a minimal oversampling ratio. IEEE Trans. Med. Imaging 24, 799–808.

Bianciardi, M., Fukunaga, M., van Gelderen, P., Horovitz, S.G., de Zwart, J.A., Shmueli, K., Duyn, J.H., 2009. Sources of functional magnetic resonance imaging signal fluctuations in the human brain at rest: a 7 T study. Magn. Reson. Imaging 27, 1019–1029. http://dx.doi.org/10.1016/j.mri.2009.02.004.

Birn, R.M., Smith, M.A., Jones, T.B., Bandettini, P.A., 2008. The respiration response function: the temporal dynamics of fMRI signal fluctuations related to changes in respiration. NeuroImage 40, 644–654. http://dx.doi.org/10.1016/j.neuroimage.2007.11.059.

Biswal, B., Zerrin Yetkin, F., Haughton, V.M., Hyde, J.S., 1995. Functional connectivity in the motor cortex of resting human brain using echo-planar MRI. Magn. Reson. Med. 34, 537–541. http://dx.doi.org/10.1002/mrm.1910340409.

Börnert, P., Schomberg, H., Aldefeld, B., Groen, J., 1999. Improvements in spiral MR imaging. Magn. Reson. Mater. Phys. Biol. Med. 9, 29–41. http://dx.doi.org/10.1007/BF02634590.

Buckner, R.L., Krienen, F.M., Yeo, B.T.T., 2013. Opportunities and limitations of intrinsic functional connectivity MRI. Nat. Neurosci. 16, 832–837. http://dx.doi.org/10.1038/nn.3423.

Carp, J., 2012. The secret lives of experiments: methods reporting in the fMRI literature. NeuroImage 63, 289–300. http://dx.doi.org/10.1016/j.neuroimage.2012.07.004.

Chang, C., Glover, G.H., 2011. Variable-density spiral-in/out functional magnetic resonance imaging. Magn. Reson. Med. 65, 1287–1296. http://dx.doi.org/10.1002/mrm.22722.

Chang, C., Cunningham, J.P., Glover, G.H., 2009. Influence of heart rate on the BOLD signal: the cardiac response function. NeuroImage 44, 857–869. http://dx.doi.org/10.1016/j.neuroimage.2008.09.029.

Cole, D.M., Smith, S.M., Beckmann, C.F., 2010. Advances and pitfalls in the analysis and interpretation of resting-state fMRI data. Front. Syst. Neurosci. 4, 1–15. http://dx.doi.org/10.3389/fnsys.2010.00008.

Dagli, M.S., Ingeholm, J.E., Haxby, J.V., 1999. Localization of cardiac-induced signal change in fMRI. NeuroImage 9, 407–415. http://dx.doi.org/10.1006/nimg.1998.0424.

De Zanche, N., Barmet, C., Nordmeyer-Massner, J.A., Pruessmann, K.P., 2008. NMR probes for measuring magnetic fields and field dynamics in MR systems. Magn. Reson. Med. 60, 176–186.

Friston, K.J., 2007. Chapter 2 - Statistical parametric mapping. In: Friston, K.J., Ashburner, J., Kiebel, S., Nichols, T., Penny, W. (Eds.), Statistical Parametric Mapping. Academic Press, London, pp. 10–31.

Glover, G.H., Lai, S., 1998. Self-navigated spiral fMRI: interleaved versus single-shot. Magn. Reson. Med. 39, 361–368. http://dx.doi.org/10.1002/mrm.1910390305.

Glover, G.H., Li, T.Q., Ress, D., 2000. Image-based method for retrospective correction of physiological motion effects in fMRI: RETROICOR. Magn. Reson. Med. 44, 162–167 (doi:10893535).

Goense, J., Merkle, H., Logothetis, N.K., 2012. High-resolution fMRI reveals laminar differences in neurovascular coupling between positive and negative BOLD responses. Neuron 76, 629–639. http://dx.doi.org/10.1016/j.neuron.2012.09.019.

Graedel, N.N., Vannesjo, S.J., Kasper, L., Gross, S., Dietrich, B.E., Barmet, C., Pruessmann, K.P., 2013. Image Reconstruction Using the Gradient Impulse Response for Trajectory Prediction. Presented at the ISMRM, Salt Lake City, USA, p. 552.

Greiser, A., von Kienlin, M., 2003. Efficient k-space sampling by density-weighted phase-encoding. Magn. Reson. Med. 50, 1266–1275. http://dx.doi.org/10.1002/mrm.10647.

Greiser, A., Haase, A., von Kienlin, M., 2005. Improved cardiac sodium MR imaging by density-weighted phase-encoding. J. Magn. Reson. Imaging 21, 78–81. http://dx.doi.org/10.1002/jmri.20237.

Hall, J., 2011. Linear Deming Regression - File Exchange - MATLAB Central [WWW Document]. (URL http://www.mathworks.com/matlabcentral/fileexchange/file_infos/33484-linear-deming-regression (accessed 8.16.13)).

Harrison, L.M., Penny, W., Flandin, G., Ruff, C.C., Weiskopf, N., Friston, K.J., 2008. Graph-partitioned spatial priors for functional magnetic resonance images. NeuroImage 43, 694–707. http://dx.doi.org/10.1016/j.neuroimage.2008.08.012.

Harvey, A.K., Pattinson, K.T.S., Brooks, J.C.W., Mayhew, S.D., Jenkinson, M., Wise, R.G., 2008. Brainstem functional magnetic resonance imaging: disentangling signal from physiological noise. J. Magn. Reson. Imaging 28, 1337–1344. http://dx.doi.org/10.1002/jmri.21623.

Haynes, J.-D., Rees, G., 2006. Decoding mental states from brain activity in humans. Nat. Rev. Neurosci. 7, 523–534. http://dx.doi.org/10.1038/nrn1931.

Hutton, C., Josephs, O., Stadler, J., Featherstone, E., Reid, A., Speck, O., Bernarding, J., Weiskopf, N., 2011. The impact of physiological noise correction on fMRI at 7 T. NeuroImage 57, 101–112. http://dx.doi.org/10.1016/j.neuroimage.2011.04.018.

Jackson, J.I., Meyer, C.H., Nishimura, D.G., Macovski, A., 1991. Selection of a convolution function for Fourier inversion using gridding. IEEE Trans. Med. Imaging 10, 473–478. http://dx.doi.org/10.1109/42.97598.

Johnson, J.B., 1928. Thermal agitation of electricity in conductors. Phys. Rev. 32, 97–109. http://dx.doi.org/10.1103/PhysRev.32.97.

Kasper, L., Marti, S., Vannesjö, S.J., Hutton, C., Dolan, R., Weiskopf, N., Stephan, K.E., Prüssmann, K.P., 2009. Cardiac Artefact Correction for Human Brainstem fMRI at 7 Tesla. Presented at the HBM, San Francisco. Proceedings of the Organization for Human Brain Mapping, 15, p. 395.

Kasper, L., Vannesjo, S.J., Haeberlin, M., Barmet, C., Stephan, K.E., Pruessmann, K.P., 2010. Non-uniform density EPI acquisition improves the SNR of smoothed MR images. Presented at the ISMRM, Stockholm, Sweden. Proc. Intl. Soc. Mag. Reson. Med., 18, p. 3040.

Kasper, L., Haeberlin, M., Wilm, B.J., Stephan, K.E., Pruessmann, K.P., 2012. 2D Matched-filter Acquisition for Improved SNR in Routine Brain Imaging. Presented at the ISMRM, Melbourne, Australia. Proc. Intl. Soc. Mag. Reson. Med., 20, p. 2299.

Kim, D., Adalsteinsson, E., Spielman, D.M., 2003. Simple analytic variable density spiral design. Magn. Reson. Med. 50, 214–219. http://dx.doi.org/10.1002/mrm.10493.

Kimmlingen, R., Eberlein, E., Dietz, P., Kreher, S., Schuster, J., Riegler, J., Matschl, V., Schnetter, V., Schmidt, A., Lenz, H., Mustafa, E., Fischer, D., Potthast, A., Kreischer, L., Eberler, M., Hebrank, F., Thein, H., Heberlein, K., Hoecht, P., Witzel, T., Tisdall, D., Xu, J., Yacoub, E., Adriany, G., Auerbach, E., Moeller, S., Feinberg, D., Lehne, D., Wald, L.L., Rosen, B., Ugurbil, K., Essen, D. van, Wedeen, V., Schmitt, F., 2012. Concept and realization of high strength gradients for the Human Connectome Project. Presented at the ISMRM, Melbourne, Australia. Proc. Intl. Soc. Mag. Reson. Med., 20, p. 696.

Koopmans, P.J., Barth, M., Norris, D.G., 2010. Layer-specific BOLD activation in human V1. Hum. Brain Mapp. 31, 1297–1304. http://dx.doi.org/10.1002/hbm.20936.

Krüger, G., Glover, G.H., 2001. Physiological noise in oxygenation-sensitive magnetic resonance imaging. Magn. Reson. Med. 46, 631–637. http://dx.doi.org/10.1002/mrm.1240.

Lindquist, M.A., Wager, T.D., 2008. Spatial smoothing in fMRI using prolate spheroidal wave functions. Hum. Brain Mapp. 29, 1276–1287. http://dx.doi.org/10.1002/hbm.20475.

Lustig, M., Kim, S.-J., Pauly, J.M., 2008. A fast method for designing time-optimal gradient waveforms for arbitrary k-Space trajectories. IEEE Trans. Med. Imaging 27, 866–873. http://dx.doi.org/10.1109/TMI.2008.922699.

Lutti, A., Thomas, D.L., Hutton, C., Weiskopf, N., 2013. High-resolution functional MRI at 3 T: 3D/2D echo-planar imaging with optimized physiological noise correction. Magn. Reson. Med. 69, 1657–1664. http://dx.doi.org/10.1002/mrm.24398.

Man, L.C., Pauly, J.M., Macovski, A., 1997. Multifrequency interpolation for fast off-resonance correction. Magn. Reson. Med. 37, 785–792 (doi:9126954).

North, D.O., 1963. An Analysis of the factors which determine signal/noise discrimination in pulsed-carrier systems. Proc. IEEE 51, 1016–1027. http://dx.doi.org/10.1109/PROC.1963.2383.

Nyquist, H., 1928. Thermal agitation of electric charge in conductors. Phys. Rev. 32, 110–113. http://dx.doi.org/10.1103/PhysRev.32.110.

Pipe, J., Duerk, J.L., 1995. Analytical resolution and noise characteristics of linearly reconstructed magnetic resonance data with arbitrary k-space sampling. Magn. Reson. Med. 34, 170–178. http://dx.doi.org/10.1002/mrm.1910340207.

Poldrack, R.A., Fletcher, P.C., Henson, R.N., Worsley, K.J., Brett, M., Nichols, T.E., 2008. Guidelines for reporting an fMRI study. NeuroImage 40, 409–414. http://dx.doi.org/10.1016/j.neuroimage.2007.11.048.

Poser, B.A., Koopmans, P.J., Witzel, T., Wald, L.L., Barth, M., 2010. Three dimensional echo-planar imaging at 7 Tesla. NeuroImage 51, 261–266. http://dx.doi.org/10.1016/j.neuroimage.2010.01.108.

Pruessmann, K., Tsao, J., 2008. United States Patent: 7342397 - Magnetic resonance imaging method. 7342397.

Pruessmann, K.P., Weiger, M., Börnert, P., Boesiger, P., 2001. Advances in sensitivity encoding with arbitrary k-space trajectories. Magn. Reson. Med. 46, 638–651. http://dx.doi.org/10.1002/mrm.1241.

Salvado, O., Hillenbrand, C., Zhang, S., Wilson, D.L., 2006. Method to correct intensity inhomogeneity in MR images for atherosclerosis characterization. IEEE Trans. Med. Imaging 25, 539–552. http://dx.doi.org/10.1109/TMI.2006.871418.

Shmueli, K., van Gelderen, P., de Zwart, J.A., Horovitz, S.G., Fukunaga, M., Martijn Jansma, J., Duyn, J.H., 2007. Low frequency fluctuations in the cardiac rate as a source of variance in the resting-state fMRI BOLD signal. NeuroImage 38, 306–320. http://dx.doi.org/10.1016/j.neuroimage.2007.07.037.

Spielman, D.M., Pauly, J.M., Meyer, C.H., 1995. Magnetic resonance fluoroscopy using spirals with variable sampling densities. Magn. Reson. Med. 34, 388–394. http://dx.doi.org/10.1002/mrm.1910340316.

Stobbe, R., Beaulieu, C., 2008. Advantage of sampling density weighted apodization over postacquisition filtering apodization for sodium MRI of the human brain. Magn. Reson. Med. 60, 981–986. http://dx.doi.org/10.1002/mrm.21738.

Sutton, B.P., Noll, D.C., Fessler, J.A., 2003. Fast, iterative image reconstruction for MRI in the presence of field inhomogeneities. IEEE Trans. Med. Imaging 22, 178–188. http://dx.doi.org/10.1109/TMI.2002.808360.

Tabelow, K., Polzehl, J., Voss, H.U., Spokoiny, V., 2006. Analyzing fMRI experiments with structural adaptive smoothing procedures. NeuroImage 33, 55–62. http://dx.doi.org/10.1016/j.neuroimage.2006.06.029.

Triantafyllou, C., Hoge, R.D., Wald, L.L., 2006. Effect of spatial smoothing on physiological noise in high-resolution fMRI. NeuroImage 32, 551–557. http://dx.doi.org/10.1016/j.neuroimage.2006.04.182.

Van De Ville, D., Blu, T., Unser, M., 2006. Surfing the brain. IEEE Eng. Med. Biol. Mag. 25, 65.

Van Essen, D.C., Ugurbil, K., Auerbach, E., Barch, D., Behrens, T.E.J., Bucholz, R., Chang, A., Chen, L., Corbetta, M., Curtiss, S.W., Della Penna, S., Feinberg, D., Glasser, M.F., Harel, N., Heath, A.C., Larson-Prior, L., Marcus, D., Michalareas, G., Moeller, S., Oostenveld, R., Petersen, S.E., Prior, F., Schlaggar, B.L., Smith, S.M., Snyder, A.Z., Xu, J., Yacoub, E., 2012. The Human Connectome Project: A data acquisition perspective. NeuroImage 62, 2222–2231. http://dx.doi.org/10.1016/j.neuroimage.2012.02.018.

Vannesjo, S.J., Dietrich, B.E., Pavan, M., Brunner, D.O., Wilm, B.J., Barmet, C., Pruessmann, K.P., 2013a. Field camera measurements of gradient and shim impulse responses using frequency sweeps. Magn. Reson. Med. http://dx.doi.org/10.1002/mrm.24934.

Vannesjo, S.J., Haeberlin, M., Kasper, L., Pavan, M., Wilm, B.J., Barmet, C., Pruessmann, K.P., 2013b. Gradient system characterization by impulse response measurements with a dynamic field camera. Magn. Reson. Med. 69, 583–593. http://dx.doi.org/10.1002/mrm.24263.

Weisstein, E.W., 2006a. "Parseval's theorem." From MathWorld–A Wolfram Web Resource. [WWW Document]. URL http://mathworld.wolfram.com/ParsevalsTheorem.html (accessed 6.27.13b).

Weisstein, E.W., 2006b. "Wiener-Khinchin theorem." From MathWorld–A Wolfram Web Resource. [WWW Document]. URL http://mathworld.wolfram.com/Wiener-KhinchinTheorem.html (accessed 6.27.13a).

Wilm, B.J., Barmet, C., Pavan, M., Pruessmann, K.P., 2011. Higher order reconstruction for MRI in the presence of spatiotemporal field perturbations. Magn. Reson. Med. 65, 1690–1701. http://dx.doi.org/10.1002/mrm.22767.

Wilm, B.J., Barmet, C., Pruessmann, K.P., 2012. Fast higher-order MR image reconstruction using singular-vector separation. IEEE Trans. Med. Imaging 31, 1396–1403. http://dx.doi.org/10.1109/TMI.2012.2190991.

Worsley, K.J., Marrett, S., Neelin, P., Evans, A.C., 1996a. Searching scale space for activation in PET images. Hum. Brain Mapp. 4, 74–90. http://dx.doi.org/10.1002/(SICI)1097-0193(1996) (4:1<74::AID-HBM5>3.0.CO;2-M).

Worsley, K.J., Marrett, S., Neelin, P., Vandal, A.C., Friston, K.J., Evans, A.C., 1996b. A unified statistical approach for determining significant signals in images of cerebral activation. Hum. Brain Mapp. 4, 58–73. http://dx.doi.org/10.1002/(SICI)1097-0193(1996) (4:1<58::AID-HBM4>3.0.CO;2-O).

Yang, Q.X., Lindquist, M.A., Shepp, L., Zhang, Cun-Hui, Wang, J., Smith, M.B., 2002. Two dimensional prolate spheroidal wave functions for MRI. J. Magn. Reson. 158, 43–51. http://dx.doi.org/10.1016/S1090-7807(02)00058-7.

Zahneisen, B., Hugger, T., Lee, K.J., LeVan, P., Reisert, M., Lee, H.-L., Assländer, J., Zaitsev, M., Hennig, J., 2012. Single shot concentric shells trajectories for ultra fast fMRI. Magn. Reson. Med. 68, 484–494. http://dx.doi.org/10.1002/mrm.23256.

Zeller, M., Müller, A., Gutberlet, M., Nichols, T., Hahn, D., Köstler, H., Bartsch, A.J., 2013. Boosting BOLD fMRI by k-space density weighted echo planar Imaging. PLoS ONE 8, e74501. http://dx.doi.org/10.1371/journal.pone.0074501.